Thesis for the degree of Doctor of Philosophy

Inverse and optimization problems in electromagnetics – a finite-element method perspective

Johan Winges

CHALMERS

Department of Signals and Systems
Signal Processing Group
chalmers university of technology
Göteborg, Sweden, 2016

Inverse and optimization problems in electromagnetics – a finite-element method perspective

Johan Winges

Doktorsavhandlingar vid Chalmers Tekniska Högskola
ISBN 978-91-7597-472-9
Series No. 4153
ISSN 0346-718X

Signal Processing Group
Department of Signals and Systems
Chalmers University of Technology
SE-412 96 Göteborg, Sweden
Telephone: +46 (0)31-772 1000

Cover:
Hybrid mesh of a $2\,\mathrm{m} \times 3\,\mathrm{m} \times 2\,\mathrm{m}$ rectangular metal cavity with 45°-chamfers along two edges where the colored tubes show the electric field lines for a resonant mode. The thickness of the tubes is proportional to the field strength and the color indicates the value of the z-coordinate.

This thesis has been prepared using LaTeX

Printed by Chalmers Reproservice
Göteborg, Sweden, 2016

There is a computer disease that anybody
who works with computers knows about.
It's a very serious disease and it
interferes completely with the work.
The trouble with computers is
that you 'play' with them!

Richard P. Feynman

ABSTRACT

In this thesis, a selection of inverse and optimization problems are studied where the finite element method (FEM) serves as a comprehensive tool to solve electromagnetic field problems that lack an analytic solution. The inverse problems are typically formulated in terms of an optimization problem where the misfit between a measurement and the corresponding result of a computational model is minimized. The optimization problems are solved by a combination of techniques that involve gradient-based methods, stochastic methods and parameter studies.

The first contribution of the thesis is a new higher-order hybrid FEM for Maxwell's equations that combines (i) brick-shaped elements for large homogeneous regions with (ii) tetrahedrons for regions where local refinement is necessary. The tangential continuity of the electric field at the interface between the different element types is enforced in the weak sense using Nitsche's method. This yields a flexible and efficient computational method that is free of spurious solutions and features a low dispersion error. We employ a stable implicit-explicit time-stepping scheme using an implicitness parameter associated with the tetrahedrons and the hybrid interface. No late-time instabilities are observed in the solution for computations with up to 300 000 time steps.

The second contribution of this thesis deals with four inverse scattering problems: (i) gradient-based estimation of the dielectric properties of moist micro-crystalline cellulose in terms of a Debye model; (ii) detection and positioning of multiple scatterers inside a metal vessel using compressed sensing; (iii) monitoring of the material perturbations in a pharmaceutical process vessel using a linearized model around an operation point that varies with the process state; and (iv) a subspace-based classification method for the detection of intracranial bleedings in a simulated data set.

The third contribution of the thesis explores stochastic optimization for an inductive power transfer (IPT) system consisting of four magnetically coupled resonance circuits, which is intended for power transfer distances on the order of the coils' radius. A genetic algorithm is employed to compute the Pareto front that contrast the maximum efficiency and power transfer. Results are presented for both linear and non-linear circuits: (i) a time-harmonic model for magnetically coupled resonance circuits with a resistive load; and (ii) a transient model for an IPT system with square-wave excitation, rectifier, smoothing filter and battery.

Keywords: computational electromagnetics, brick-tetrahedron hybrid, finite element method, microwave measurements, optimization, inverse problems, parameter estimation, compressed sensing, inductive power transfer, wireless power

LIST OF PUBLICATIONS

This thesis is based on and includes the following publications:

I **J. Winges** and T. Rylander, "Higher-order brick-tetrahedron hybrid method for Maxwell's equations in time domain," *Journal of Computational Physics*, vol. 321, p. 698-707, 2016.

II L. Cerullo, **J. Winges**, T. Rylander, T. McKelvey, L. Gradinarsky, S. Folestad and M. Viberg, "Microwave Measurement System for Dispersive Dielectric Properties of Densely Packed Pellets," *to be submitted to Measurement*, 2016

III **J. Winges**, L. Cerullo, T. Rylander, T. McKelvey and M. Viberg, "Compressed sensing for the detection and positioning of dielectric objects inside metal enclosures by means of microwave measurements," *in manuscript*, 2016

IV J. Nohlert, L. Cerullo, **J. Winges**, T. Rylander, T. McKelvey, A. Holmgren, L. Gradinarsky, S. Folestad, M. Viberg, A. Rasmuson, "Global Monitoring of Fluidized-Bed Processes by means of Microwave Cavity Resonances," *Measurement*, vol. 55, p. 520-535, 2014.

V S. Candefjord, **J. Winges**, A. A. Malik, Y. Yu, T. Rylander, T. McKelvey, A. Fhager, M. Elam, M. Persson, "Microwave Technology For Detecting Traumatic Intracranial Bleedings," *Medical & Biological Engineering & Computing*, In press, 2016.

VI **J. Winges**, T. Rylander, C. Petersson, C. Ekman, L.-Å. Johansson and T. McKelvey, "Multi-objective optimization of wireless power-transfer system with magnetically coupled resonators and non-linear load," *in manuscript*, 2016.

Other related publications and presentations by the author not included in this thesis:

- L. Cerullo, **J. Winges**, T. Rylander, T. McKelvey, L. Gradinarsky, M. Viberg and S. Folestad, "Inverse scattering for a closed cavity equipped with microwave antenna sensors," *Poster presented at AntennEMB*, 2012.
- Y. Yu, **J. Winges**, T. McKelvey, and T. Rylander, "Model reduction for inverse scattering problems," *Poster presented at AntennEMB*, 2012.
- L. Cerullo, J. Nohlert, **J. Winges**, T. Rylander, T. McKelvey, L. Gradinarsky, M. Viberg and S. Folestad, "Microwave Measurements for Metal Vessels," *Proceedings of the 7th European Conference on Antennas and Propagation, EuCAP*, 2013.
- S. Candefjord, **J. Winges**, Y. Yu, T. Rylander, T. McKelvey, "Microwave technology for localization of traumatic intracranial bleedings – A numerical simulation study," *Proceedings of the 35th International Conference on Engineering in Medicine and Biology Society, EMBC*, 2013.
- **J. Winges**, "Microwave Measurement Systems for Parameter Estimation and Classification," *Licentiate thesis*, R009/2014, ISSN 1403-266X, Dept. of Signals and systems, Chalmers University of Technology, 2014.
- **J. Winges** and T. Rylander, "Higher-Order Finite Element Solver for Maxwell's Equations," *Poster presented at AntennEMB*, 2014.
- **J. Winges** L. Cerullo, T. Rylander, T. McKelvey, L. Gradinarsky, S. Folestad and M. Viberg, "A Microwave Measurement System for Measurement of Dielectric Properties," *Poster presented at AntennEMB*, 2014.
- **J. Winges** and T. Rylander, "Higher-order hybrid method for curl-conforming elements on tetrahedrons and bricks," *Proceedings of the International Conference on Electromagnetics in Advanced Applications, ICEAA*, p. 1016-1019, 2015.
- **J. Winges** and T. Rylander, "Estimating Scatterer Positions using Sparse Approximation," *Presentation at Swedish Microwave days, AntennEMB*, 2016.
- **J. Winges** and T. Rylander, "Sparse Approximation for Microwave Measurements - Estimation of the Number of Scatterers and their Positions," *Presentation at Compressed Sensing Workshop, Lund*, 2016.

ACKNOWLEDGMENTS

I would like to express my gratitude to a number of people. Your help and support have been greatly appreciated during the last five years.

- First and foremost, my supervisor Thomas Rylander. During the years we have had a great collaboration in various interesting and exciting research subjects. Your experience and insight have been greatly appreciated.
- Next, my co-authors. In particular, Johan Nohlert, Livia Cerullo, Tomas McKelvey and Stefan Candefjord. Thanks for the opportunity of interesting and fruitful research collaborations.
- Also, the signal processing group, of which I have been a part of during my research at Chalmers. I have had a lot of great moments during social activities, group meetings as well as during coffee and lunch breaks.
- In addition to the research group, I enjoyed many great discussions during coffee and lunch with many friends in the department of signals and systems. These discussions have been invaluable and greatly appreciated.
- Finally, all my other friends and family. In particular, Jessica and the cats.

This PhD position have been financially supported by the Swedish Research Council (dnr 2010-4627) in the project ”Model-based Reconstruction and Classification Based on Near-Field Microwave Measurements” and the Swedish Energy Agency in the project ”Safe Wireless Energy” (FFI 38577-1). Computations were performed on resources at Chalmers Center for Computational Science and Engineering (C3SE) provided by the Swedish National Infrastructure for Computing (SNIC). Astra Zeneca is acknowledged for the support in terms of experimental data and measurement campaigns featured in this thesis.

Johan Winges
September, 2016

CONTENTS

CHAPTER 1

INTRODUCTION

Design and optimization based on computational technology is a powerful and versatile tool in electrical engineering for a broad range of applications. The rapid development of computers and the accessibility of computer clusters paves the way for approaching increasingly challenging problems. However, the advancement of numerical methods and algorithms for electromagnetic problems is of equally large importance and the main topic of this thesis. The thesis also presents the design, optimization and analysis of a few electromagnetic applications. In particular, we use microwave technology to measure and detect permittivity variations and design a wireless energy transfer system for charging batteries in the automotive industry.

1.1 Computational electromagnetics

The theory of electromagnetism is classically expressed by Maxwell's equations and there exists a number of computational methods that may be used to solve electromagnetic field problems. The finite-differences time-domain (FDTD) scheme and the finite element method (FEM) are two important and well-known methods that are suitable for electromagnetic field problems where the computational domain features different dielectric properties and metal parts. An introduction to these methods can be found in the textbook [1].

The finite-differences time-domain (FDTD) scheme [2, 3] is a popular numerical method for solving electromagnetic problems on structured grids. The FDTD scheme is an efficient method due to its matrix free implementation, which uses an explicit "leap-frog" time-stepping scheme with a maximum allowed time-step according to the Courant condition [1]. However, for the lowest-order approximation, the FDTD scheme suffers from significant dispersion errors that makes the numerical solution inaccurate for electromagnetically large problems. Higher-order FDTD schemes on staggered grids have been developed [4,5] and they greatly reduce the dispersion errors, which allows for larger computational domains (in terms of wavelengths). Unfortunately, the use of structured grids introduces quite large discretization errors due to the staircase approximation of oblique and curved boundaries.

The finite element method (FEM) has some of its earliest applications in structural engineering and have since the introduction of edge-basis functions by Nédélec [6] been extensively used for electromagnetic problems [7]. In contrast to the FDTD scheme, the FEM can be formulated for unstructured meshes[1] that allow for accurate representation of oblique and curved boundaries. For edge elements, unstructured meshes yield non-diagonal mass matrices and typically require implicit time-stepping schemes. The implicit time-stepping can, however, be made unconditionally stable for all element sizes and, consequently, render the time step independent on the spatial resolution. Thus, unstructured meshes facilitate for relatively inexpensive local mesh refinement that may be necessary for fine geometrical details or for regions with rapid field variations. Moreover, higher-order hierarchical basis functions [8,9] can be used to improve the accuracy of the solution, and they allow for local control of the basis functions' polynomial order p for different parts of the computational domain (in addition to refinement in the element size h). Similarly to the FDTD scheme[2], the FEM can also be formulated for structured grids using brick-shaped elements. For brick-shaped elements, it is possible to use higher-order basis functions with mass-lumping [10] to achieve a diagonal mass matrix. Then, explicit time-stepping schemes can be used with a computational efficiency on par with the higher-order FDTD schemes.

An attractive solution to efficiently handle large computational domains that feature small geometrical details is to construct hybrid methods that combine structured grids for the large homogeneous regions with unstructured meshes only where it is necessary. Rylander and Bondesson presented in [11] a curl-conforming lowest-order hybrid FEM that connects brick-shaped elements to tetrahedral elements by a layer of pyramids. In addition, a stable implicit-explicit time-stepping scheme is presented in [11] which features an implicitness parameter associated with each element. An appropriate choice of the implicitness parameters yields a global time-stepping scheme that is limited by the Courant condition for the brick-shaped elements and unconditionally stable for the remaining element types. Mesh generation is, however, inconvenient for the hybrid with pyramids and higher-order basis function on pyramids are difficult to construct, although some progress have been made recently [12]. Another hybrid FEM that connects the brick-shaped elements directly to the tetrahdrons have been presented by Degerfeldt et al. [13] for the lowest-order elements. The lowest-order brick and tetrahedral elements feature different incomplete first-order[3] polynomial bases and this results in a discontinuous tangential electric field at the hybrid interface. For the hybrid method presented by Degerfeldt, the degrees of freedom for the field at the hybrid interface are related in the strong sense such that the resulting hybrid method is free from spurious solutions. A higher-order hybrid brick-tetrahedron method have been presented by Marais et al. [14]. This hybrid method requires tetrahedral elements at the hybrid interface with complete-order basis

[1]Unstructured meshes are typically constructed using tetrahedral elements in three-dimensions and triangles in two-dimensions.

[2]Employing trapezoidal integration for the lowest-order brick-shaped elements with explicit time-stepping yields a FEM computationally identical to the lowest-order FDTD scheme.

[3]An *incomplete* first-order basis is not linear in all field components.

functions that features degrees of freedom that do not contribute to the modeling of the curl of the electric field. Marais uses in [14] a strong coupling for each element at the hybrid interface and point-wise tangential continuity of the electric field is achieved, at the expense of solving multiple projection problems with the extra degrees of freedom. In this thesis, a higher-order brick-tetrahedron FEM is presented in **Paper I**, which enforces tangential continuity of the electric field at the hybrid interface in the weak sense by means of Nitsche's method [15]. This approach allows for the representation of the electric field using incomplete-order basis functions for the tetrahedral elements at the hybrid interface and, consequently, fewer degrees of freedom.

1.2 Design, optimization and analysis

Computational technology provide vital tools for the design, optimization and analysis of electromagnetic devices. An especially important tool in optimization is sensitivity analysis, which relates perturbations of the geometry or the material properties to perturbations in the electromagnetic field. Sensitivities are widely employed for gradient-based optimization of the shape or the material parameters of, e.g., microwave devices and antennas [16, 17]. Gradient-based optimization is also used to solve inverse scattering problems related to reconstruction and imaging [18,19] and in the estimation of material parameters, which is attempted in **Paper II** and **IV**. Moreover, sensitivities can also be used to find uncertainties in the estimated parameters (see **Paper II**). Regular finite-differences can be used to compute sensitivities at the cost of (at least) one additional simulation for each parameter of interest. A more attractive and efficient method is to employ an adjoint field formulation [20]. Using the adjoint field solution it is possible to compute the sensitivities with respect to all parameters of interest at once.

Gradient-based optimization are difficult to use for problems that feature many local optima or situations with a varying or an unknown number of parameters to be determined. An attractive alternative is then to employ global stochastic optimization methods [21], such as genetic algorithms or particle swarm optimization. Stochastic methods do in general not rely on sensitivities, and instead use random perturbations of the design parameters based on, e.g., evolutionary inspired selection, breeding and mutation. In practice, stochastic methods may not necessarily converge to the global optimum as they can prematurely converge to a local optimum. It is, therefore, often advantageous to perform a few subsequent optimizations for the same problem to increase the likelihood that the global optimum has been found. For optimization problems that need to be solved repeatedly or in a limited amount of time, an attractive alternative to stochastic methods are grid-based approaches, where a look-up table or dictionary is computed for the expected parameter variations. Generally, the look-up search can be fast, but the accuracy of the grid-based approach can be severely limited by the discretization of the parameters in the look-up table, unless suitable interpolation can be employed.

Compressed sensing [22] has since its conception become a popular method to deal with certain electromagnetic problems [23]. Currently, compressed sensing is often used for direction-of-arrival (DOA) estimation and radar imaging [24, 25] where a sparse set of sources or scattering objects far from the antennas are determined. In addition, compressed sensing is also used for sparse antenna array synthesis and fault detection in antenna arrays [26, 27], and some recent advances show promise for near-field microwave imaging of sparse material distributions [28]. Compressed sensing is based on the assumption that the underlying measured signal can be represented as sparse in a suitably selected basis [22], and sparsity is often enforced by penalizing the 1-norm of the solution [29]. A remarkable strength of compressed sensing is that considerably fewer sample points are necessary compared to the Nyquist's sampling rate for sparse signals [30].

1.3 Microwave technology

Microwave technology is an important component of electrical engineering with a multitude of applications in, for example, the process industry, biomedicine, communication and astronomy. An integral part of microwave technology are microwave measurements using different types of microwave sensors. Nyfors [31] presents an excellent survey of common microwave sensors and their operation for applications in the industry and for research purposes. A great range of microwave measurement applications are also available in the literature: (i) humidity sensors [32]; (ii) moisture content measurement in pharmaceutical powders and in paper [33, 34]; (iii) microwave tomography for brain and breast imaging [19, 35]; (iv) distance and velocity sensors for vehicles [36]; (v) decay detection in living trees [37].

Microwave measurements can often be classified as non-intrusive and non-destructive, which are important attributes for monitoring and detection systems in the process industry and in biomedical applications. The rapid development and miniaturization of microwave equipment have also made microwave measurements a portable and cost-effective alternative or compliment to other measurement techniques such as metal detectors, ultrasonic sensors, X-rays and magnetic resonance imaging (MRI) systems. As microwaves interact strongly with water [32], large dielectric contrasts may be observed between materials with different amount of moisture content. This facilitates for sensitive and accurate moisture detection and monitoring, which is attempted in **Paper II** and **IV**. In biomdedicial applications, large dielectric contrasts can also be observed between different types of tissue. For example, the conductive losses between blood and gray mater differ substantially [38], making microwave measurements an attractive tool for intracranial bleeding detection (see **Paper V**). A possible limitation of microwave measurements is that the spatial resolution generally depends on the wavelength. In the literature, resolutions on the order of $\lambda/30$ have been reported for simple targets using multiple near-fieldmeasurements [39], where λ is the wavelength. In the far-field, the resolution is limited by $\lambda/2$ according to the Rayleigh criterion [40]. However, super resolution can be possible for sparse targets using compressed sensing [25, 41]. Compressed sensing may thus offer increased resolution and positioning accuracy for microwave measurements that feature an underlying sparsity, which is attempted in **Paper III** for the detection and positioning of a sparse set of scatterers inside a metal vessel.

1.4 Wireless power transfer

Wireless power transfer between a power source and a receiving electric device is generally categorized as non-radiative or radiative. For short distances, non-radiative techniques has the potential for high power transfer at high efficiency with low sensitivity to misalignment issues. The most common non-radiative technique for short to mid-range distances is inductive power transfer [42], altough some progress in capacitive power transfer has been made [43, 44].

Inductive power transfer (IPT) is generally based on magnetically coupled coils and has received increased attention during the last decades for short to mid-range distances [45]. Short-range wireless charging systems for medical implants [46, 47], mobile phones and laptops [48] have been developed and affordable products exists on the market today. Mid-range IPT systems typically uses resonant coils or circuits with high quality factors Q. The relatively high Q-values of the resonators allow for the storage of non-radiative electromagnetic energy in the vicinity of the source coil, which can be efficiently picked up by the device coil if it is tuned to the same resonant frequency. In particular, Kurs et al. demonstrated in [49] a 60 W power transfer at 40 % efficiency over the considerable distance of 2 m, or roughly eight times the radius of the coils. This was achieved using two self-resonant coils with a resonance frequency of 9.9 MHz and a quality factor of about 950. A practical issue with the resonant mid-range inductive power transfer is the de-tuning of the source or device resonator, which is a difficult problem to solve due to the necessity of high quality factors to achieve high efficiency. Moreover, as the distance between the source and the device is reduced, the magnetic coupling increases and a complicated coupled resonator behavior can be observed, where it may be necessary to compensate for phenomena such as frequency splitting [50, 51]. Additional resonant coils (or resonant circuits) have been proposed to achieve higher power transfer and increased efficiency, and it is common to consider a setup of four or more resonant coils [50–52]. Analytic derivations are, however, much more complex for the multi-coil setup. Typically, assumptions on the optimal resonance frequencies and approximations on the cross-coupling between coils are used to arrive at manageable formulas, which may produce sub-optimal designs in real applications.

An important application for short to mid-range IPT is wireless charging systems for batteries in electric or hybrid vehicles [42, 53, 54]. Wireless power can increase the availability and convenience of battery charging systems, which can make it possible to use smaller and cheaper batteries in electric vehicles and, consequently, make electric vehicles a more attractive alternative to vehicles using fossil fuels. An overview of the power transfer as a function of the relative transfer distance d as compared to the maximum radius $r_{\max}$ of the system is shown in Figure 1.1 for a few selected references and a 3.7 kW IPT system with $d/r_{\max} = 1.2$ presented in **Paper VI**. It is clear from Figure 1.1 that the realizable power transfer decreases substantially with increasing transfer distances (for a given system size) in the literature. In **Paper VI**, we present optimized designs for a prototype IPT system with four air-wound circular coils. We consider an IPT system capable of transferring power over distances between about 20 cm to 30 cm using coils with a radius of no larger than 25 cm, where these dimensions are expected constraints for a vehicle parked above a charging station located in the ground. Further, motivated

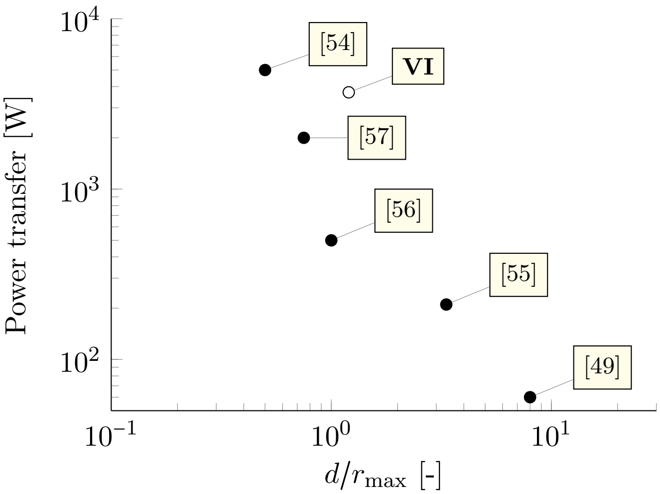

Figure 1.1: Overview of achieved power transfer as a function of the transfer distance d divided by the maximum radius $r_{\max}$ of the physical dimension for some IPT systems presented in the literature and for the results presented in **Paper VI**.

by the SAE standard [58], we consider an operational frequency of 85 kHz and attempt to realize a power transfer of at least 3.7 kW at an efficiency of preferably above 95 %, which may be necessary to compete with regular charging using cables. In addition, we note that the magnetic field strengths must conform with regulations and guidelines in places where humans may be present in a realized IPT system. For example, the ICNIRP guidlines from 1998 specifies that the general public should not be exposed to more than 6.25 μT at frequencies between 1 kHz to 150 kHz [59]. This constraint on the magnetic field strength in combination with component constraints in terms of maximum allowed voltages and currents make the design and operation of IPT systems for vehicular charging an interesting challenge.

CHAPTER 2

HIGHER-ORDER FEM FOR HYBRID MESHES

Higher-order finite element methods (FEM) in computational electromagnetics are very appealing as they yield low dispersion errors, which is important for electrically large problems. In addition, the FEM can handle complex geometry and complicated constitutive relations that often are featured in real-world applications. In order to address this family of problems, we have constructed a higher-order brick-tetrahedron hybrid FEM, which is presented in **Paper I**. This method combines the geometry modeling capabilities of tetrahedrons with the computational efficiency of bricks to create an efficient and flexible computational method for Maxwell's equations.

2.1 Higher-order brick-tetrahedron hybrid method for Maxwell's equations

A higher-order brick-tetrahedron hybrid method for Maxwell's equations is presented in **Paper I**. The method is based on the FEM which is a flexible framework to construct reliable and efficient computational methods for electromagnetic problems [1, 7, 10]. The method combines brick-shaped and tetrahedral elements that are connected at a hybrid interface Γ (see Figure 2.1). The tangential continuity for the electric field at Γ is enforced in the weak sense using Nitsche's method [15]. The brick-shaped elements are useful for large homogeneous regions as they allow for mass-lumping, explicit time-stepping and matrix-free computer implementations [10]. The tetrahedral elements provide an important complement since they can model complex geometries and are suitable for local mesh refinement. The utilization of higher-order basis functions yields low discretization errors proportional to h^{2p} (where h is the element size and p is the basis function order) for regular problems that do not feature re-entrant edges or corners.

To conveniently formulate the hybrid method, the second-order differential equation for the electric field in the frequency domain is considered [60]. Thus, we seek the electric

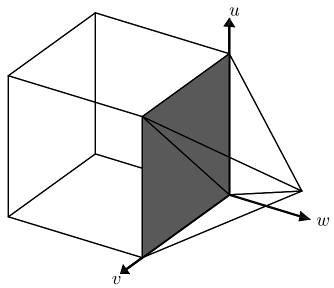

Figure 2.1: Hybrid interface in dark gray between a brick-shaped element and two tetrahedrons.

field $\boldsymbol{E}(\boldsymbol{r},\omega)$ that satisfies

$$\begin{aligned} \nabla \times \nabla \times \boldsymbol{E} - \mu_0 \epsilon \omega^2 \boldsymbol{E} &= \boldsymbol{0} && \text{in } \Omega, && (2.1a)\\ \hat{\boldsymbol{n}} \times \boldsymbol{E} &= \boldsymbol{0} && \text{on } \partial\Omega, && (2.1b)\\ \hat{\boldsymbol{n}} \times [\![\boldsymbol{E}]\!] &= \boldsymbol{0} && \text{on } \Gamma, && (2.1c)\\ \hat{\boldsymbol{n}} \times [\![\nabla \times \boldsymbol{E}]\!] &= \boldsymbol{0} && \text{on } \Gamma, && (2.1d) \end{aligned}$$

where $[\![\boldsymbol{E}]\!] = \boldsymbol{E}^{\text{bse}} - \boldsymbol{E}^{\text{tet}}$ is the jump of $\boldsymbol{E}$ at the interface Γ and $\Omega = \Omega^{\text{tet}} \cup \Omega^{\text{bse}}$ is the computational domain with an outer boundary $\partial\Omega$. For simplicity, the outer boundary is modeled as a perfect electric conductor (PEC).

A conventional curl-conforming representation of the electric field ensures that the tangential continuity condition in Eq. (2.1c) hold for all element interfaces. An example is the lowest-order curl-conforming hybrid FEM method that connects regions of brick-shaped elements and tetrahedral elements using a layer of pyramids [11]. Unfortunately, the edge basis functions for the pyramids are non-polynomial, which makes error analysis difficult and it may be inconvenient to handle mesh generation for this hybrid. In addition, it is difficult to construct higher-order basis functions for pyramids, although some recent results are available [61].

The combination of elements shown in Figure 2.1 does not necessarily yield a curl-conforming representation of the electric field at the hybrid boundary. For the lowest-order brick-tetrahedron hybrid method (without a layer of pyramids), Degerfeldt et al. [13] showed that it is possible to connect the two types of elements at the hybrid interface in the strong sense for the discretization shown in Figure 2.1. The hybrid method presented in **Paper I** employs higher-order basis functions for the brick-shaped and the tetrahedral elements. The tangential continuity of the electric field at Γ is enforced in the weak sense using Nitsche's method, which features a stabilization parameter γ that can be chosen. This construction makes it possible to represent the electric field in terms of both incomplete- or complete-order basis functions for the tetrahedrons, where the complete-order basis functions could be suitable for problems with strong gradient fields. This formulation is free from spurious modes and it yields an error proportional to h^{2p} for regular problems. In addition, it allows for stable hybrid implicit-explicit time-stepping.

2.1.1 Weak form

We expand the electric field in curl-conforming basis functions $\boldsymbol{N}_i$ and use Galerkin's method in conjunction with Nitsche's method to derive a consistent weak form of Eq. (2.1) as

$$\begin{aligned}
&\left(\nabla \times \boldsymbol{N}_i^{\text{tet}}, \nabla \times \boldsymbol{E}^{\text{tet}}\right)_{\Omega^{\text{tet}}} + \left(\nabla \times \boldsymbol{N}_i^{\text{bse}}, \nabla \times \boldsymbol{E}^{\text{bse}}\right)_{\Omega^{\text{bse}}} - \left(\hat{\boldsymbol{n}} \times [\![\boldsymbol{N}_i]\!], \{\!\{\nabla \times \boldsymbol{E}\}\!\}_\alpha\right)_\Gamma \\
&- \left(\{\!\{\nabla \times \boldsymbol{N}_i\}\!\}_\alpha, \hat{\boldsymbol{n}} \times [\![\boldsymbol{E}]\!]\right)_\Gamma + \gamma \left(\hat{\boldsymbol{n}} \times [\![\boldsymbol{N}_i]\!], h^{-1}\hat{\boldsymbol{n}} \times [\![\boldsymbol{E}]\!]\right)_\Gamma \\
&= \mu_0\epsilon_0\omega^2 \left[\left(\boldsymbol{N}_i^{\text{tet}}, \epsilon_r \boldsymbol{E}^{\text{tet}}\right)_{\Omega^{\text{tet}}} + \left(\boldsymbol{N}_i^{\text{bse}}, \epsilon_r \boldsymbol{E}^{\text{bse}}\right)_{\Omega^{\text{bse}}}\right] .
\end{aligned} \tag{2.2}$$

Here, $\gamma \geq 0$ is a stabilization parameter that governs the tangential continuity of the electric field at the interface (in the weak sense) when sufficiently large. For convenience, we define the corresponding stiffness and mass matrices from the weak form (2.2)

$$S_{i,j}^{\text{tet}} = \left(\nabla \times \boldsymbol{N}_i^{\text{tet}}, \nabla \times \boldsymbol{N}_j^{\text{tet}}\right)_{\Omega^{\text{tet}}} , \tag{2.3a}$$

$$S_{i,j}^{\text{bse}} = \left(\nabla \times \boldsymbol{N}_i^{\text{bse}}, \nabla \times \boldsymbol{N}_j^{\text{bse}}\right)_{\Omega^{\text{bse}}} , \tag{2.3b}$$

$$S_{i,j}^{\Gamma} = \left(\hat{\boldsymbol{n}} \times [\![\boldsymbol{N}_i]\!], \{\!\{\nabla \times \boldsymbol{N}_j\}\!\}_\alpha\right)_\Gamma + \left(\{\!\{\nabla \times \boldsymbol{N}_i\}\!\}_\alpha, \hat{\boldsymbol{n}} \times [\![\boldsymbol{N}_j]\!]\right)_\Gamma , \tag{2.3c}$$

$$S_{i,j}^{\Gamma_s} = \left(\hat{\boldsymbol{n}} \times [\![\boldsymbol{N}_i]\!], h^{-1}\hat{\boldsymbol{n}} \times [\![\boldsymbol{N}_j]\!]\right)_\Gamma , \tag{2.3d}$$

$$M_{i,j} = \left(\boldsymbol{N}_i^{\text{tet}}, \epsilon_r \boldsymbol{N}_j^{\text{tet}}\right)_{\Omega^{\text{tet}}} + \left(\boldsymbol{N}_i^{\text{bse}}, \epsilon_r \boldsymbol{N}_j^{\text{bse}}\right)_{\Omega^{\text{bse}}} . \tag{2.3e}$$

For the lowest-order curl-conforming hybrid construction with tetrahedrons directly connected to bricks, the interface contributions in Eq. (2.3c) evaluate to zero [13] and, consequently, no stabilization is needed, which in turn makes the choice $\gamma = 0$ is possible.

The weak form for conventional FEM based on a globally curl-conforming representation for the electric field is a special case of the weak form in (2.2). For example, a discretization that only contains tetrahedral elements yields

$$\left(\nabla \times \boldsymbol{N}_i^{\text{tet}}, \nabla \times \boldsymbol{E}^{\text{tet}}\right)_{\Omega^{\text{tet}}} = \mu_0\epsilon_0\omega^2 \left(\boldsymbol{N}_i^{\text{tet}}, \epsilon_r \boldsymbol{E}^{\text{tet}}\right)_{\Omega^{\text{tet}}} , \tag{2.4}$$

which is used in **Paper IV** for finding the eigenfrequencies in metal cavities. Naturally, it is possible to derive similar weak forms for two-dimensional (2D) problems, where we typically employ triangular elements (see **Papers II**, **III** and **V**). We stress that additional boundary conditions for the 2D and 3D wave equation are possible to include in the derivation of the weak form. Robin boundary conditions is an important type which, e.g., can be used to model rectangular waveguides [7] (see **Papers II**, **III** and **V**).

2.1.2 Time-stepping scheme

The hybrid method is time-stepped using an implicit-explicit time-stepping scheme [11], which is based on a partitioning of the stiffness matrix into an implicit and explicit part depending on the element type. An implicitness parameter θ is associated with the tetrahedral elements and the hybrid interface and we write the hybrid time-stepping scheme as

$$\begin{aligned}&(\mathbf{S}^{\text{tet}} - \mathbf{S}^{\Gamma} + \gamma\mathbf{S}^{\Gamma_s})\left[\theta\mathbf{e}^{(n+1)} + (1-2\theta)\mathbf{e}^{(n)} + \theta\mathbf{e}^{(n-1)}\right] + \mathbf{S}^{\text{bse}}\mathbf{e}^{(n)}\\&+\frac{1}{(c_0\Delta t)^2}\mathbf{M}\left[\mathbf{e}^{(n+1)} - 2\mathbf{e}^{(n)} + \mathbf{e}^{(n-1)}\right] = 0\,,\end{aligned} \tag{2.5}$$

where $\mathbf{e}^{(n)} = \mathbf{e}(t)|_{t=n\Delta t}$ is the coefficient vector of the electric field at time step n. To achieve stability for the explicit part of the global time-stepping scheme (2.5), the time step must satisfy the Courant condition $c_0\Delta t \le 2/\sqrt{\lambda_{\max}}$ for the brick-shaped elements. The maximum eigenvalue $\lambda_{\max}$ depends on the size of the smallest brick-shaped element and the basis function order p. For a cube-shaped element of side h, the maximum eigenvalue and correspondingly allowed time step are presented in Table 2.1. The implicit

Table 2.1: Maximum eigenvalue versus (incomplete) basis order p for a single cube-shaped element of side h and the corresponding maximum allowed time step according to the Courant condition.

p	1_i	2_i	3_i	4_i
$\lambda_{\max}$	$12/h^2$	$72/h^2$	$222.94/h^2$	$550.05/h^2$
$c_0\Delta t$	$0.577h$	$0.235h$	$0.133h$	$0.085h$

part of the time-stepping scheme is unconditionally stable if $\theta \ge 1/4$, which assumes that we have a positive semi-definite stiffness matrix [11]. Here, a sufficiently large value of the stabilization parameter γ ensures a positive semi-definite stiffness matrix, which makes stable time-stepping possible.

2.1.3 Validation and results

Two resonant rectangular cavity examples are used to test and validate the presented hybrid method. First, we consider a 0.9 m × 1.0 m × 1.1 m cavity and construct a hybrid mesh as shown in Figure 2.2(a). This hybrid mesh is hierarchically refined and we perform a convergence study for our method. The hybrid method produces the expected eigenfrequency spectra (with correct multiplicity) with an error that is proportional to approximately h^{2p} using $\gamma = 10^5$. Figure 2.2(b) shows the relative error of the lowest eigenfrequency as a function of the number of elements per wavelength for polynomial order of the basis functions from one to four. A significant improvement in accuracy is achieved for higher polynomial-order of the basis functions.

The stable hybrid explicit-implicit time-stepping is demonstrated for the 2 m×3 m×2 m rectangular cavity in Figure 2.3(a) which features 45°-chamfers along two edges. For $p^{\text{tet}} = p^{\text{bse}} = 3_\text{i}$ and $\gamma = 10^5$, the hybrid time-stepping scheme is run for 300 000 time steps using $\theta = 1/4$ and the maximum Δt allowed according to the Courant condition (for the brick-shaped elements). The resulting discrete Fourier transform of some arbitrarily selected electric field components is shown in Figure 2.3(b). The computed resonance peaks agrees well with the seven lowest resonance frequencies computed by the commercial

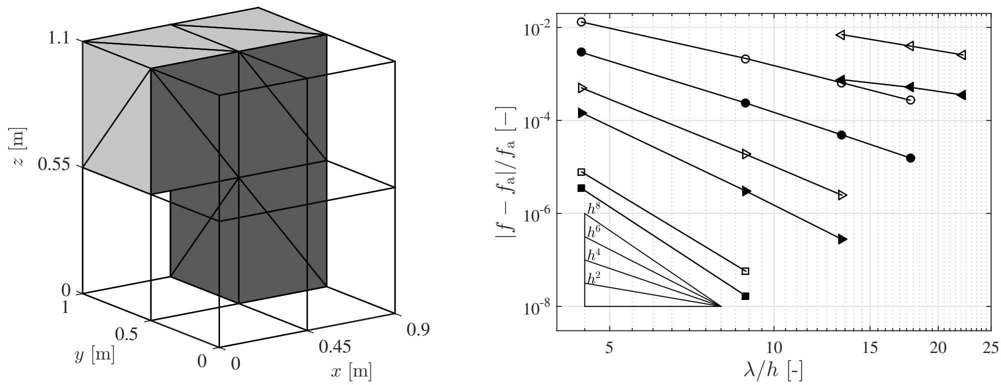

(a) Hybrid mesh **(b)** Convergence plot

Figure 2.2: **(a)** Hybrid mesh of a rectangular cavity where the hybrid interface is shown with dark gray triangles, the tetrahedral elements on the outer boundary with light gray triangles and the brick-shaped elements using transparent wire-frame boxes. **(b)** The relative error of the lowest eigenfrequency as a function of the number of elements per wavelength: hollow glyphs - incomplete-order basis for all elements; and solid glyphs - complete-order basis for (only) the tetrahedrons. Here, we have linear elements (triangles pointing to the left), quadratic elements (circles), cubic elements (triangles pointing to the right) and quartic elements (squares).

solver *COMSOL Multiphyics*® [62]. The hybrid method does not show any signs of late-time instabilities.

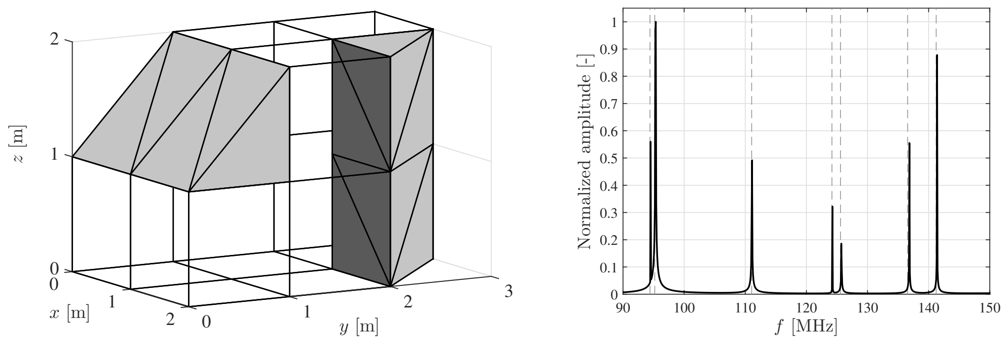

(a) Hybrid mesh **(b)** Resonance frequencies

Figure 2.3: **(a)** Hybrid mesh of a rectangular cavity with 45°-chamfers. **(b)** Discrete Fourier transform after 300 000 time steps using the hybrid method with incomplete third-order basis functions. The dashed vertical lines are the seven lowest eigenfrequencies obtained using *COMSOL Multiphysics*®.

2.2 Material models

In pharmaceutical industry, water or moisture content is of great importance during the manufacturing process and in the final product [33]. Due to the relatively high permittivity of water for frequencies below 10 GHz, it is appealing to use electromagnetic fields for the estimation of water or moisture content in products that exhibit substantially lower permittivity for the dry product. The complex permittivity $\epsilon_{\mathrm{c}}(\omega) = \epsilon'(\omega) - j\epsilon''(\omega)$ of water may be characterized by the Debye model [63, 64]

$$\epsilon_{\mathrm{c}}(\omega) = \epsilon_0 \left(\epsilon_\infty + \frac{\epsilon_{\mathrm{s}} - \epsilon_\infty}{1 + j\omega\tau} \right), \tag{2.6}$$

where ϵ_{s}, ϵ_∞ and τ are commonly denoted as the static permittivity, the optical permittivity and the relaxation time, respectively. The Debye model yields a passive material and it satisfies the fundamental assumptions about causality.

In the pharmaceutical industry, it is common with material mixtures. For mixtures with (spherical) inclusions of considerably smaller size than the wavelength inside an otherwise homogeneous background material, an effective permittivity of the mixture, ϵ_{eff}, is practical to use. The effective permittivity ϵ_{eff} can be computed using the Maxwell-Garnett mixing formula [65], given that the permittivity of the materials involved in the mixture and the volume fraction of the inclusions are known. An important and interesting special case are powders where small particles are mixed with air. Then, if the bulk permittivity of the particles can be characterized by a Debye model (which is likely the case for materials with high moisture content), the effective permittivity of the mixture can also be characterized by a related but different Debye model. In **Paper II**, we attempt to characterize a material mixture of air and particles of microcrystalline-cellulose (MCC) with different moisture content using a Debye model, and in **Paper IV** we monitor the effective permittivity of a MCC and air mixture inside a pharmaceutical process vessel.

CHAPTER 3

OPTIMIZATION, INVERSE AND CLASSIFICATION PROBLEMS

In most engineering disciplines, optimization is an important tool to solve original design problems and improve existing constructions, which is attempted for a wireless power transfer system in **Paper VI**. In the context of inverse problems, optimization algorithms can be used to estimate parameters as demonstrated in **Papers II**, **III** and **IV**. Classification also involves elements of optimization and it is useful for separating large sets of complex data into different classes, which is tested in **Paper V** with the aim of detecting the presence of intracranial bleedings from high-dimensional microwave scattering data.

3.1 Optimization

We consider a generic objective based optimization problem with constraints and, here, we state it as a minimization problem

$$\min_{\boldsymbol{x}} g(\boldsymbol{x}) \,, \tag{3.1a}$$

$$\text{subject to: } \mathbf{l} \leq \mathbf{c}(\boldsymbol{x}) \leq \mathbf{u} \,, \tag{3.1b}$$

where $g(\boldsymbol{x})$ is the objective function and $\mathbf{c}(\boldsymbol{x})$ is an array of constraint functions with lower bounds $\mathbf{l}$ and upper bounds $\mathbf{u}$. For many engineering problems, the objective and the constraints are non-linear functions that are computationally expensive to evaluate. There are some special cases of the objective function $g(\boldsymbol{x})$ and the constraints $\mathbf{c}(\boldsymbol{x})$ that simplify the optimization problem such that the computational effort is significantly reduced. An important such case is convex optimization [66], which implies that the objective function is convex and that the constraints form a convex set. For convex minimization problems, any local minimum is also a global minimum, which facilitates for efficient solution methods such as gradient-descent [66] and interior-point methods [67]. Another important case is quadratic programming [68], which implies that the objective function can be written as a quadratic form and that the constraints are linear, i.e.

$$g(\boldsymbol{x}) = \boldsymbol{x}^T \mathbf{Q}\boldsymbol{x} + \mathbf{d}^T \boldsymbol{x} \quad \text{and} \quad \mathbf{c}(\boldsymbol{x}) = \mathbf{A}\boldsymbol{x}\,. \tag{3.2}$$

Quadratic minimization problems are convex if $\mathbf{Q}$ is a positive semi-definite matrix [66].

There exists a large number of methods for solving the optimization problem (3.1). Three important classes of optimization methods are (i) gradient-based, (ii) stochastic, and (iii) grid-based approaches. Gradient-based methods utilizes the gradient of the objective function, $\nabla_{\boldsymbol{x}} g(\boldsymbol{x})$, to find an appropriate search direction for the variables $\boldsymbol{x}$ which reduces the value of the objective function [69]. The use of the gradient yields an efficient and fast method that converges to a local optimum, which depends on the initial guess. Gradient-based methods can have difficulties in finding a global optimum for problems with many local optima, whereas they excel at solving convex problems.

Stochastic optimization methods [21], e.g. genetic algorithms or particle swarm optimization, attempt to improve a set of candidate solutions. These methods do not in general rely on the gradient or some other assumptions on the objective function, and instead use randomness with an often biologically inspired fitness based selection criterion as a means to solve the optimization problem. This approach can solve many optimization problems given enough time, but can be very computationally costly due to the large number of function evaluations required. Other issues are that stochastic methods may not necessarily converge to the same solution every time, and that the convergence time can be quite unpredictable.

In grid-based approaches, the objective function is computed for a parameterization of the parameters $\boldsymbol{x}$ and the result stored in a table or dictionary. This approach allows for finding an approximate solution to the optimization problem using for example a fast look-up or search procedure, which may be necessary to perform optimization in real-time constrained applications. Even if embarrassingly parallel, the computational cost of constructing the dictionary may be substantial. However, if the same dictionary can re-used to solve multiple optimization problems, the overall computational effort may become smaller than if, e.g, a gradient-based method is used for each of the individual optimization problems. Grid-based approaches are usually only feasible for relatively low-dimensional parameter spaces with a limited number of discretization points in each dimension. This is because the number of computations typically scale exponentially with the number of dimensions.

3.1.1 Multi-objective optimization

Multi-objective optimization [70] considers the simultaneous minimization of several objective functions $g_1(\boldsymbol{x}), \ldots, g_N(\boldsymbol{x})$ subject to constraints $\mathbf{l} \leq \mathbf{c}(\boldsymbol{x}) \leq \mathbf{u}$. Typically, the objective functions are conflicting, and there exists a potentially infinite number of Pareto-optimal solutions[1]. The set of Pareto-optimal solutions is referred to as the Pareto front and it can be computed by a posteriori methods [71]. Popular methods to compute the

[1] A Pareto-optimal solution is such that none of the objective functions can be further decreased without increasing at least one of the other objective functions

Pareto front include mathematical programming with weighting schemes[2] and genetic algorithms [72]. As any point on the Pareto front is a Pareto-optimal solution, additional information is often used in the design stage to select the most advantageous optimum.

3.2 Inverse problems

Inverse problems [73] are an important class of problems that are often encountered when we attempt to estimate parameters from a measurement. Typically, the measurement $\overline{\mathbf{m}}$ is the result of an unknown cause represented by the parameters $\boldsymbol{x}$ and a mathematical model $\mathbf{m}(\boldsymbol{x})$ describing the physics of the system. The objective is then to determine $\boldsymbol{x}$ such that at least approximately $\overline{\mathbf{m}} = \mathbf{m}(\boldsymbol{x})$. This parameter estimation problem can be framed as an optimization problem with the objective function

$$g(\boldsymbol{x}) = \|\mathbf{m}(\boldsymbol{x}) - \overline{\mathbf{m}}\| \tag{3.3}$$

where $\|\cdot\|$ is a suitably selected norm, often the Euclidean 2-norm.

Many inverse problems are ill-posed. An ill-posed problem violates at least one of Hadamard's three conditions for well-posed problems [74]: (i) the solution exists; (ii) the solution is unique; and (iii) the solution changes continuously with the data. A well-posed problem stands a good chance to be solved using a stable algorithm. Ill-posed problems generally require some additional regularization to stabilize the solution even if a stable algorithm is employed. Typically, a priori information about the inverse problem such as the noise level, parameter dependencies or solution features, e.g., $\boldsymbol{x}$ is smooth or sparse, can be included as regularization and help guide the algorithm to a more realistic solution.

In electromagnetic applications, the mathematical model $\mathbf{m}(\boldsymbol{x})$ is generally based on solving Maxwell's equations. The measurement $\overline{\mathbf{m}}$ is typically a number of scattering parameters or the resonance frequencies in a frequency band of interest. From the measured quantities $\overline{\mathbf{m}}$, we are interested in estimating $\boldsymbol{x}$, which can for example describe the dielectric properties of a material or a material distribution, or the position or shape of a scattering object. One method to estimate $\boldsymbol{x}$ is to employ gradient-based optimization to solve (3.3), where the gradients can be efficiently computed using an adjoint field formulation [75] (see **Paper II** for details). Another possibility is that we know a priori that only small perturbations around some known point $\boldsymbol{x}_0$ is expected. For such cases it is appropriate to linearize the model as

$$\mathbf{m}(\boldsymbol{x}) \simeq \mathbf{m}_0 + \nabla_{\boldsymbol{x}}\mathbf{m}|_{\boldsymbol{x}_0}(\boldsymbol{x} - \boldsymbol{x}_0)\,. \tag{3.4}$$

The resulting optimization problem can then be stated as a convex quadratic problem, which simplifies the optimization and facilitates for a fast (potentially real-time) parameter estimation. In **Paper IV**, we employ this method and attempt to monitor a process vessel where certain parameters drift over time by continuously updating the linearization

[2]For two objectives, the Pareto front can be described as the minimum value of the weighted sum $g(\boldsymbol{x}) = \alpha g_1(\boldsymbol{x}) + (1-\alpha)g_2(\boldsymbol{x})$, where $0 \le \alpha \le 1$ is the weight.

point.

An attractive method that can be used to efficiently solve certain optimization problems is compressed sensing [22, 23]. The standard compressed sensing paradigm is based on the following two requirements: (i) the relation between the unknowns $\boldsymbol{x}$ and the data $\mathbf{m}$ is linear; and (ii) the unknown vector $\boldsymbol{x}$ is sparse[3] [29]. Typically, a dictionary $\mathbf{D}$ is used to represent the linear relationship between the unknowns and the data as $\mathbf{m} = \mathbf{D}\boldsymbol{x}$. A sparse solution can be computed which approximates a measurement $\overline{\mathbf{m}}$ as $\mathbf{D}\boldsymbol{x}$ by minimizing the objective function

$$g(\boldsymbol{x}) = \|\mathbf{D}\boldsymbol{x} - \overline{\mathbf{m}}\|_2 + \gamma\|\mathbf{W}\boldsymbol{x}\|_1 \,, \tag{3.5}$$

where γ is a penalization parameter which penalizes the 1-norm of $\boldsymbol{x}$ [29] and $\mathbf{W}$ a weight matrix. Compared to penalizing the 0-norm, the 1-norm penalization has the attractive feature that the resulting optimization problem is convex. Moreover, if all parameters $\boldsymbol{x}$ are non-negative, the objective function (3.5) may be formulated as a quadratic optimization problem for linear constraints. Unfortunately, electromagnetic inverse scattering problems are generally non-linear in terms of the dielectric properties of the material distribution that we wish to determine. However, superposition approximations or reformulations [76] can yield a linear or approximately linear inverse scattering problem that may be possible to solve using compressed sensing. In **Paper III**, we employ compressed sensing and a superposition approximation and attempt to detect and estimate the positions of multiple scatterers simultaneously by neglecting higher-order scattering effects between the individual scatterers.

3.3 Classification

There is an important family of measurement problems where the task is to make a decision based on a number of distinct options, rather than to estimate a set of quantities or parameters. For such decision-making situations, classification techniques can extract useful information from data that is difficult to otherwise directly analyze and draw conclusions from. Typically, a classification algorithm is trained on a set of labeled training data. Then, the algorithm is expected to perform well on new (previously unseen) data points [77]. Generally, the accuracy of a classifying algorithm is increased the more training data is supplied and, in many real-world situations, the difficulty to obtain a sufficient amount of training data may be challenging. In addition, verifying that the classifier works is key and large additional validation data sets are often required to reduce problems related to over fitting.

Scattering data from microwave measurements are complex high dimensional data that may involve a variety of signal paths and frequencies. In contrast to inverse scattering problems, a classification algorithm works directly on the raw scattering data and learns how it relates to a few specified classes of interest. A subspace-based classification algorithm [78] is employed in **Paper V**, and it is used to classify large sets of simulated

[3]Sparsity is generally measured by the 0-norm and a vector with only a S non-zero elements is referred to as S-sparse.

microwave scattering data from a 2D model of a human head into the classes healthy or suffering from an intracranial bleeding.

CHAPTER 4

APPLICATIONS AND RESULTS

4.1 Microwave tomography system

A microwave measurement system intended for testing and validation of two inverse scattering algorithms is shown in Figure 4.1. Specifically, the system is used to (i) estimate the dielectric properties of microcrystalline-cellulose (MCC) powders with different levels of moisture and (ii) detect and position scatterers. The measurement system consists of a metal cavity connected to six rectangular waveguides, where each waveguide is connected via an adapter to a coaxial cable. This yields a well-defined measurement region which is shielded from external sources that may disturb the measurement. A network analyzer and switch is used to automatically measure the 6-by-6 scattering matrix at the coaxial ports. The measurement system can be operated in the frequency band from 2.7 GHz to 5.1 GHz, where the excitation of the six different waveguide ports yields 21 unique signal paths (due to reciprocity).

4.1.1 Modeling and calibration

The rectangular waveguides and their intersection can be described as a two-dimensional (2D) electromagnetic field problem for the vertical electric field $\boldsymbol{E} = \hat{z}E_z(x,y)$ if $\epsilon = \epsilon(x,y)$. This 2D electromagnetic field problem is solved by a conventional FEM with triangular elements and higher-order node-based elements for the z-component of the electric field. The computational domain is bounded by PEC except for the rectangular waveguide ports, which are modeled by a Robin boundary condition [7].

The waveguide-to-coaxial adapters in Figure 4.1(a) are not included in the computational 2D model. However, **Paper II** and **III** presents a technique for dealing with this issue and it is described below. To model their effect, we use six identical 2-by-2 scattering matrices $\mathbf{S}^{\mathrm{a}}$ for the adapters. The adapters are assumed to be reciprocal and we determine the set of coefficients that describe the adapters' scattering matrix in a least-squares sense for each frequency separately using a system model when the mea-

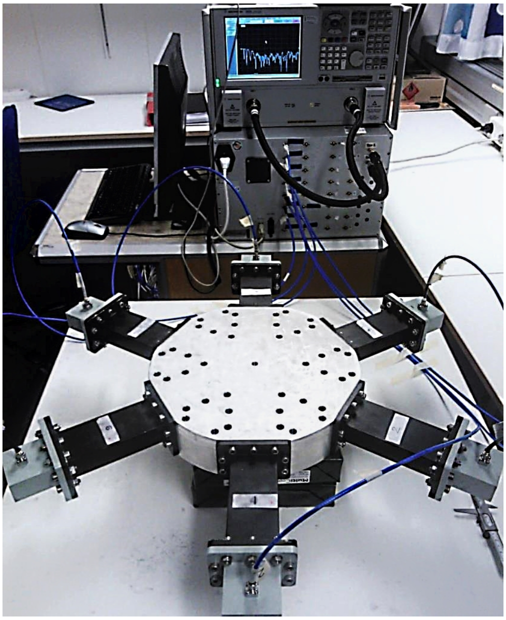

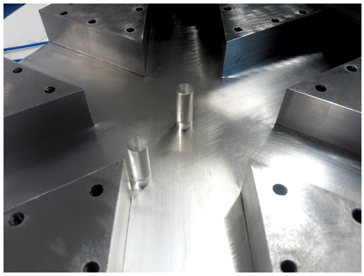

(b) Two samples

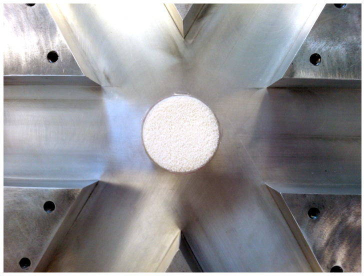

(a) Closed measurement system

(c) MCC powder

Figure 4.1: (a) Photo of the (closed) microwave measurement system connected to a network analyzer and switch. The interior of the measurement system is shown in **(b)** with two acrylic-glass samples and in **(c)** with a plastic container filled with microcrystalline-cellulose (MCC) powder.

surement region is filled with only air. In the system model, the computed scattering parameters at the rectangular waveguide ports are related to the measured scattering parameters at the coaxial waveguide ports by means of the scattering parameters of the adapters.

4.1.2 Estimation of material permittivity

A common material in the manufacturing of drugs in the pharmaceutical industry is MCC powders. The moisture content of the MCC powder is a critical parameter to control during the manufacturing process and consequently an important quantity to estimate and monitor [33]. In **Paper II**, we use the microwave measurement system shown in Figure 4.1 to estimate the dielectric properties of MCC powder for four different levels of moisture. A thin plastic beaker is used to contain the MCC powder inside the measurement system as shown in Figure 4.1(c). We characterize the (unknown) dielectric properties of the MCC powder using a few different dispersive material models for the region inside the beaker. The Debye model described in Section 2.2 is particularly well-suited for material mixtures with high moisture contents.

We estimate the parameters describing the dielectric properties by solving the resulting inverse scattering problem using a gradient-based optimization method. In particular, we minimize the root-mean-square misfit between the measured and simulated scattering parameters over the frequency band from 2.7 GHz to 5.1 GHz. The resulting complex permittivity as a function of frequency is shown in Figure 4.2 for MCC with a moisture content of 9.2 mass-percent for four different dispersive material models: (i) Debye model; (ii) Cole-Cole model; (iii) Cole-Davidson model; and (iv) a simple model with piecewise constant ϵ in small frequency bins. All considered material models yield similar results for the complex permittivity over the frequency band of interest and show similarities with earlier results in the literature for MCC mixtures [33]. The corresponding Debye

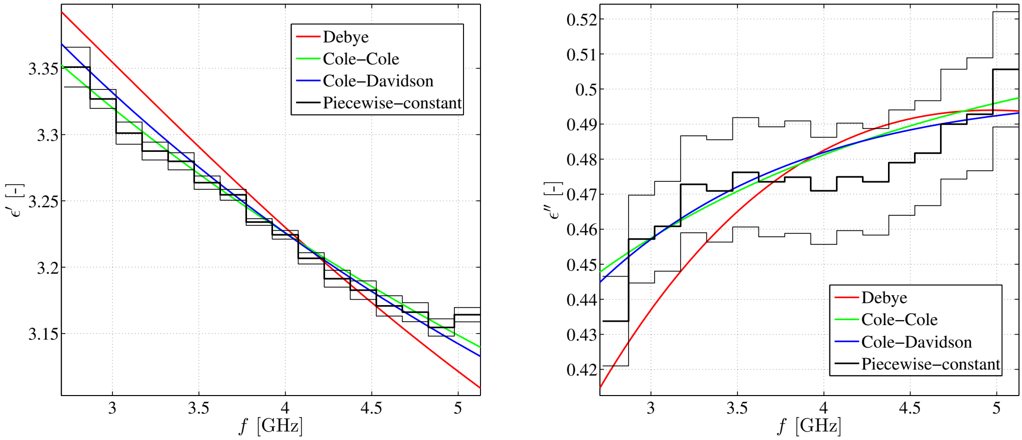

(a) Real part **(b)** Imaginary part

Figure 4.2: Estimated complex permittivity for MCC with 9.2 mass-percent moisture content using four different dispersive material models. For the piecewise constant model, the thin upper and lower curves are an estimate of the uncertainty, here about 1 % to 4 %.

parameters are presented in Table 4.1 for four different moisture contents, and we note a clear dependence between (i) the moisture content and (ii) the static permittivity and the relaxation time. The uncertainties of the Debye parameters presented in Table 4.1 are

Table 4.1: Estimated Debye parameters for packed MCC powder at four different moisture contents for the frequency band 2.7 GHz to 5.1 GHz.

Moisture	ϵ_s [-]	ϵ_∞ [-]	τ [ps]
9.2 %	3.62 ± 0.02	2.63 ± 0.03	32.0 ± 0.9
12.2 %	4.27 ± 0.04	2.85 ± 0.05	24.2 ± 0.8
16.8 %	4.88 ± 0.05	2.79 ± 0.12	15.5 ± 0.8
22.8 %	5.49 ± 0.07	2.36 ± 0.26	10.3 ± 0.8

computed using sensitivities with respect to the expected uncertainties in other model parameters such as the beaker position, permittivity and radius as well as from an estimate of the measurement noise. The details about the permittivity and uncertainty estimation is presented in **Paper II**.

4.1.3 Detection and positioning of scatterers

In **Paper III**, we use the microwave system shown in Figure 4.1 to detect and position one to five dielectric scatterers placed inside the measurement region using compressed sensing. The scatterers considered are acrylic-glass cylinders (see Figure 4.1(b)), which have a diameter of about 1 cm and a relative permittivity of about 2.5.

The compressed sensing approach utilizes a pre-computed dictionary with the microwave response for a single scatterer (i.e. a dielectric cylinder with the a priori known diameter and permittivity), where different columns in the dictionary correspond to the scatterer placed at different positions inside the measurement region. A sparse approximation in terms of the dictionary is computed for a measured microwave response by solving a convex optimization problem where the 1-norm of the solution is penalized. The non-zero elements $\hat{x}_k$ form clusters that agree rather well with the actual scatterer positions, which is shown in Figure 4.3 for two representative examples where three scatterers are present inside the measurement system and the non-zero elements are shown by colored dots. The estimated position $\hat{\mathbf{p}}$ for each scatterer is computed as a weighted

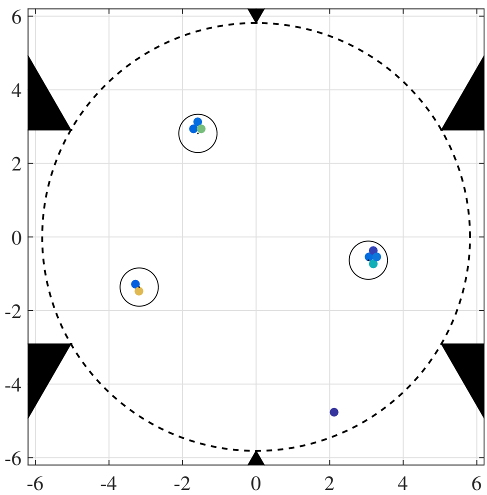

(a) [cm]

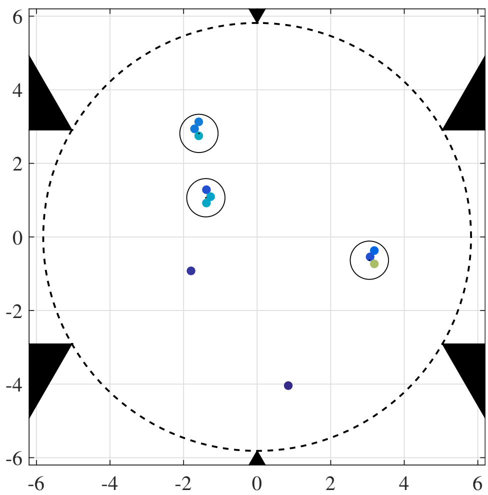

(b) [cm]

Figure 4.3: The colored dots show the positions of the estimated non-zero weights $\hat{x}_k$ for two different measurements with three acrylic-glass samples, where the outer radius of the samples are marked with a solid line. The circular measurement region is marked with a thick dashed circle and the metal in between the waveguides are marked in black. The color of the dots indicate the values of the weights, where dark blue indicate a low value near zero and light colors a value closer to one.

average of each cluster according to

$$\hat{\mathbf{p}} = \frac{\sum_k \hat{x}_k \mathbf{p}_k}{\sum_k \hat{x}_k}, \tag{4.1}$$

where the index k corresponds to a column in the dictionary that is generated for a scatterer position $\mathbf{p}_k$ with the estimated weight $\hat{x}_k$. This weighted average can yield positions in between the positions of the grid points used in the dictionary and a short derivation and motivation of this formula is presented in **Paper III**.

We find that this compressed sensing based approach is accurate using only about 10 to 20 frequency points in the frequency band 2.7 GHz to 4.2 GHz, which can facilitate for fast measurements and real-time monitoring. The method correctly identifies the number of scatterers and their positions for five or less scatterers, if the scatterers are well separated. Should two scatterers be located too close to each other, the compressed sensing method yields a single cluster that is placed in-between the scatterers, where the total weight of the cluster is close to the sum of the two scatterers.

4.2 Monitoring of pharmaceutical process vessel using microwave resonances

In certain drug manufacturing stages in the pharmaceutical industry, small particles are sprayed and coated with thin layers of different substances inside a fluidized-bed processes vessel. During the coating procedure, the moisture content of the particle and air mixture inside the process vessel is important to keep within certain bounds to assure that the end product is of high quality and that a low variation between production batches is achieved. In **Paper IV**, we present a microwave based monitoring system for a lab-scale fluidized-bed process vessel of Wurster type shown in Figure 4.4.

The process vessel is mainly made of metal and the monitoring system exploits the microwave cavity resonances inside the process vessel, which are excited by means of two H-probes connected to a network analyzer (see Figure 4.4(a) and 4.4(b)). The H-probes couple to eight usable resonant modes in the frequency range 0.75 GHz to 1.5 GHz. These resonant modes have Q-values in the range from 3 000 to 10 000. The different field patterns of the modes yield different sensing characteristics for different parts of the interior of the process vessel. Thus, the monitoring system is sensitive to both local and global changes in the permittivity distribution inside the process vessel.

4.2.1 Modeling and calibration

An accurate geometrical model of the interior of the process vessel is constructed with discrete regions as shown in Figure 4.4(c). The resonance frequencies of the process vessel are computed as a function of probable permittivity values in the bed-region using a curl-conforming FEM with first order tetrahedral elements (see Eq. (2.4) for the corresponding weak form). In addition, the sensitivities of the resonance frequencies with respect to permittivity changes are computed for all the discretized regions as well as versus shape

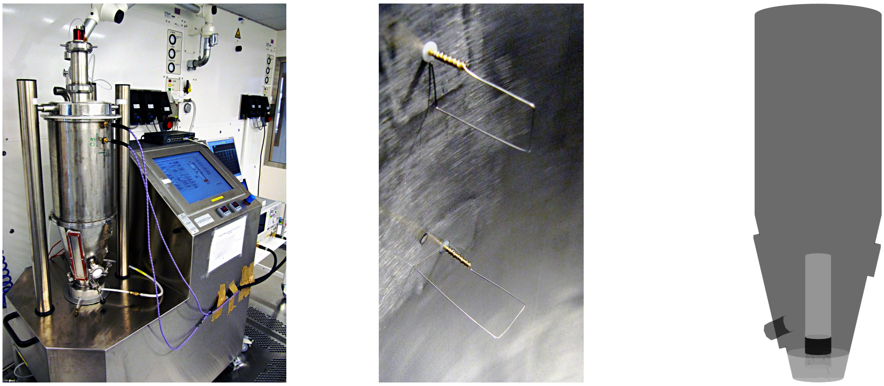

(a) System **(b)** H-probes **(c)** Discretization

Figure 4.4: (a) Photo of a lab-scale fluidized-bed system with two coaxial connections for microwave measurements. **(b)** Close-up view of the two sensing H-probes inside the process vessel. **(c)** A schematic representation of the discretization of the interior volume into fluidized bed (light gray bottom part), Wurster tube (black), particle fountain (light gray) and the remaining volume inside the vessel (dark gray).

deformations of the wall of the process vessel, where the hypothesis is that the shape (and size) of the process vessel may change due to the temperature changes of the air inside the vessel during operation.

The estimation of the permittivity in each of the discretized regions is based on finding permittivity perturbations around an appropriate linearization point such that the measured and simulated resonance frequencies agree. In an attempt to calibrate for differences between the simulated model and the actual system, the resonance frequencies for the empty process vessel is considered as a reference case. The relative differences of the resonance shifts compared to the reference case are then used in the estimation. During the course of the process, the effective permittivity in the fluidized-bed region may change significantly due to the coating of the particles that, consequently, grow in size. Thus, the linearization point is changed in accordance with detection of significant changes in the estimated permittivity of the bed-region.

Four temperature probes are used to measure the temperature changes of the metal wall of the process vessel at different locations due to the relatively slow heating and cooling that occurs during operation. Such variations in temperature are expected to cause thermal expansion of the vessel and, consequently, variations in the measured resonance frequencies. Thus, we attempt to establish the relation between (i) the temperature as measured by the probes and (ii) the shape deformations of the vessel as perceived by the resonance shifts. This relation is established for an experiment where only the heating and cooling mechanisms are present in an empty vessel with dry air. These (trained) temperature dependent shape deformations are included in the estimation procedure as a priori information.

4.2.2 Results

The estimated shifts in the complex permittivity in the fluidized-bed and fountain regions are shown in Figure 4.5 for a representative process scenario, where MCC particles are coated by a solution containing Mannitol and Kollicoat IR® using a slow to medium spray rate during almost one hour. Initially, the particle fountain is turned off, at which point

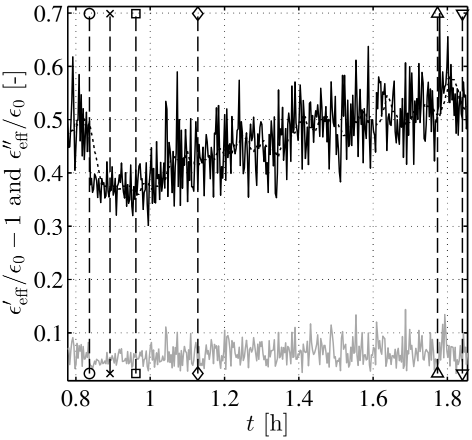

(a) Fluidized bed

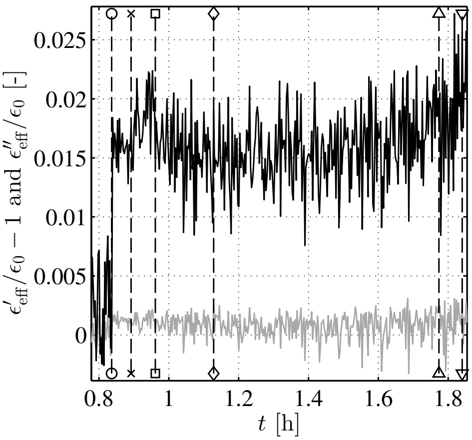

(b) Particle fountain

Figure 4.5: Estimated relative shift in complex permittivity in the bed and fountain regions as a function of process time. The dashed lines with glyphs indicate changes to the process state: first, the fountain is turned on (circles); next, the spraying of coating substance is started and increased (cross and square); and finally, the spraying stopped and fountain turned off (triangles). The diamond glyph indicate when the temperature variations due to the spraying reached a steady state.

there are almost no particles anywhere but in the fluidized-bed region. The pressurized air that drives the particle fountain is turned on at $t = 0.83$ and a clear reduction of the permittivity in the bed-region is observed while the permittivity in the particle fountain is significantly increased. This is expected as the pressurized air ejects some of the particles in the fluidized-bed through the Wurster tube after which the particles move in a fountain like pattern. A short while after the fountain is turned on, a spray is added to the pressurized air flow at an initially low rate and later increased up to 6.6 g/min at $t = 0.96$ h, which is kept fixed until $t = 1.78$ h. During this time interval, a clear increase in the effective permittivity of the bed region is observed, which is expected as the particles grow in size and the amount of material in the bed region increases. The growth of the particles was verified after the experiment was completed by means of weighing. During the process, the linearization point for the permittivity of the bed-region is changed according to the dotted line in Figure 4.5(a) (where the only clear deviation from the mean is just after the particle fountain is turned on). Additional results as well as further details about the process vessel and the monitoring system are presented in **Paper IV**.

4.3 Microwave technology for detection of traumatic intracranial bleedings

Microwave based measurement systems can offer an important compliment to traditional diagnostic techniques employed in the health care, e.g. magnetic resonance imaging (MRI) or X-ray computed tomography (CT) [79], as microwave equipment can be made portable and is relatively inexpensive in comparison. A particular important application is the detection of intracranial bleedings [80], which might occur after shock trauma in an accident. Currently, bleedings may be detected too late for proper treatment, should the patient not show any clear symptoms. Microwave technology can aid in the detection of bleedings already in the prehospital setting and could therefore help patients receive the correct treatment in time. **Paper V** describes a microwave based measurement system, which in conjunction with a classification algorithm may help in the detection of intracranial bleedings. The sub-space based classification algorithm is tested for a large set of simulated microwave scattering data for a simplified 2D model of a human head with or without bleeding surrounded by eight parallel plate waveguide antennas shown in Figure 4.6(a). The head size, bleeding position, bleeding thickness and thickness of the cerebral spinal fluid (CSF) are varied in the simulated data model to reflect inter-patient variability. In addition, a small random rotation of the head as compared to the antennas is included to model antenna misalignment.

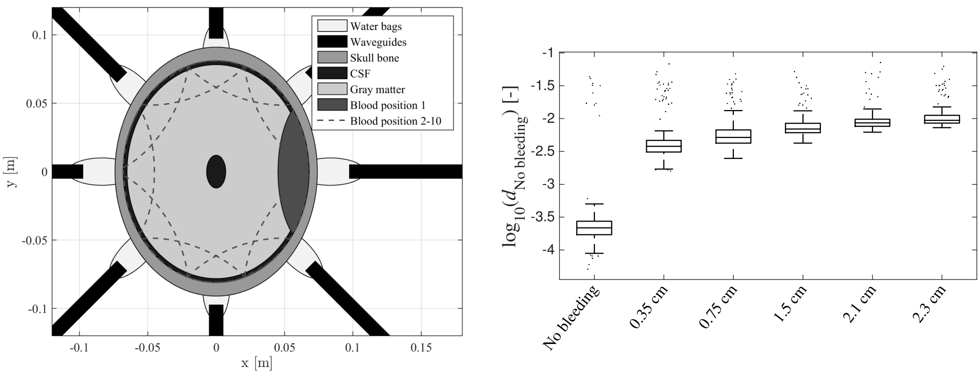

(a) 2D geometry **(b)** Subspace distance

Figure 4.6: **(a)** 2D geometry of the simplified microwave system for a head with a 2 cm thick crescent shaped bleeding. **(b)** Box plot showing the distribution of the logarithm of the subspace distance to the no bleeding class versus the different bleeding thicknesses in the validation data set.

The classifier is trained on a large data set (1250 cases) with five different bleeding thicknesses for a total of six different classes including the no bleeding case. After training, the classifier is tested on an equally large validation data set, which features head and bleeding sizes that are different as compared to the training data set. The found subspace distance between the no bleeding case and the bleeding sizes in the validation data set is presented in Figure 4.6(b). A clear correlation between subspace distance and the bleeding thickness is observed and the classifier correctly identifies bleedings with a high accuracy when trained with sufficiently large (above 150 cases per class) data sets.

4.4 Wireless power transfer system

Wireless power transfer can make battery charging more available, convenient and reliable for electric or hybrid vehicles. Inductive power transfer (IPT) system based on resonant circuits with magnetically coupled coils is particularly well-suited for high-power transfer over distances on the order of 20 cm to 30 cm, which is necessary to conveniently charge the batteries of a car parked above a charging station located in the ground. In **Paper VI**, we present a wireless charging system based on four magnetically coupled resonance circuits capable of transferring well above 3.7 kW at high efficiency over the air using circular coils at the standardized frequency 85 kHz [58].

4.4.1 Circuit and coil modeling

A circuit model for an IPT system based on four magnetically coupled resonance circuits is shown in Figure 4.7. The two sub-circuits to the left belongs to the primary side which is located in the ground. The secondary side consists of the two sub-circuits to the right and these are placed under the vehicle. The two parasitic resonance circuits with coils L_2 and L_3 yield a transfer system with significantly more flexibility than a system with only a single send and receive coil. The coils are connected to capacitor banks C_1 to C_4,

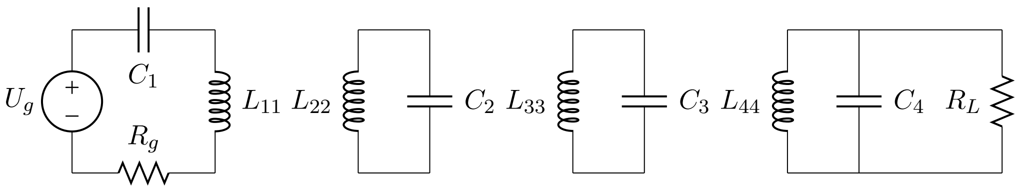

Figure 4.7: Circuit diagram for a inductive power transfer system with four coils and capacitors and a resistive load.

which makes it possible to tune the resonance frequency $f_m = 1/(2\pi\sqrt{L_{mm}C_m})$ for each inductor-capacitor sub-circuit individually. The circuit in Figure 4.7 can be solved for the time-harmonic case if the generator supplies a sinusoidal voltage $U_g = U_g^{\text{peak}}\sin(2\pi ft)$. For circular coils in free space aligned along a common axis, analytic results for the self- and mutual-inductance[1] are available in the literature [60]. This analytic coil model is computationally efficient and can demonstrate the potential of the IPT system for coupling coefficients[2] that may be comparable to a coil system placed underneath an

[1]The mutual-inductance between coil m and n is denoted L_{mn}.

[2]The coupling coefficient between coil m and n is defined as $k_{mn} = L_{mn}/\sqrt{L_{mm}L_{nn}}$ and it is a unit less quantity between zero and one.

actual vehicle[3]. Typically, a vehicle features a metallic bottom plate and, consequently, it is beneficial to use ferrite materials to guide the magnetic fields and mitigate the eddy-current losses in the metal plate. The ferrite material and the metal parts do, however, increase the overall losses for an IPT system placed underneath a vehicle as compared to the system with circular coils in air presented here.

In a real-world battery charging situation, the alternating current delivered to the load needs to be rectified. Thus, we replace the resistive load R_L in Figure 4.7 with the circuit shown in Figure 4.8, i.e. a diode bridge rectifier, a filter and a simple battery model. In addition, a DC-to-AC power inverter based on a switched H-bridge is considered as the

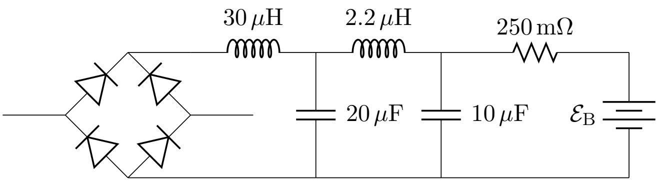

Figure 4.8: Circuit diagram for a time-dependent load consisting of rectifier, filter and a battery model with component values.

generator for the time-dependent circuit with a specified maximum voltage of 450 V. The power inverter produces a square-wave output voltage at a frequency controlled by the switching times of the H-bridge. The square-wave output voltage and the rectifier circuit can produce current overtones in the coils with non-zero amplitudes at higher multiples of the operating frequency. These currents cause magnetic fields at frequencies outside the allocated frequency band [58], and could therefore interfere with or damage other electric systems in the vehicle and potentially pose a health issue. Consequently, the current overtones should be limited and suitably constrained in the design and optimization of the IPT system.

4.4.2 Optimization and results

For single layer coils, optimization with respect to the radius of the coils, the number of turns of wire[4] in the radial direction of the coils, the coil positions and the resonance frequencies f_n is carried out to find the maximum possible power transfer and efficiency using a multiobjective genetic algorithm (GA) implemented in MATLAB [81]. The maximum radius of the coils is set to 25 cm and no more than 15 turns are allowed in each coil to assure that the maximum wire length is manageable and at least two order of magni-

[3]Two circular coils with a radius of 25 cm has a coupling coefficient in the range of 0.05 to 0.16 when separated by a distance between 20 cm to 40 cm. Similar coupling coefficients can be observed for a coil system placed underneath a vehicle that feature 50×50 cm ferrite plates behind the coils.

[4]The coil wire is a Litz wire with a radius of 5 mm, which consists of twisted and individually insulated strands of copper which yields a resistance that is approximetely equal to the direct current resistance of the copper part of the wire.

tude shorter than the wavelength at the operating frequency of 85 kHz[5]. The positions of the coils are constrained such that they all share a common axis. In addition, a minimum distance between the nearby coils is set to 17 mm to allow for a simple fixture to hold each coil, and the minimum allowed distance between the primary and secondary side is varied between 20 cm to 40 cm. To include additional losses that can be expected in an actual IPT system, a 100 mΩ contact resistance is added to each of the coil resistances in addition to the resistance of the coil wire. Further, the optimization is subject to suitable constraints for the allowed root-mean-square (rms) values of the currents and voltages across the components (see Table 4.2). If any of the constraints are violated, the generator voltage is reduced until the constraints are satisfied, which as a consequence reduces the realizable power transfer.

Table 4.2: Important constraints for the current ($i = i(t)$), current overtones ($\delta i = \delta i(t)$) and voltage ($v = v(t)$) for different circuit components in the IPT system. The constraints are stated in terms of their maximum root-meas-square (rms) values where $m = 1, \dots, 4$ indicate the component index.

Component	Quantity	Constraint
Coil (L_{mm}, R_m)	$< i >_{\mathrm{rms}}$	60 A
	$< \delta i >_{\mathrm{rms}}$	2 A
Capacitor (C_m)	$< i >_{\mathrm{rms}}$	40 A
	$< v >_{\mathrm{rms}}$	5 kV
	$< v >_{\mathrm{rms}} < i >_{\mathrm{rms}}$	50 kVA
Power inverter (R_g)	$< i >_{\mathrm{rms}}$	30 A
Rectifier (D_m)	$< i >_{\mathrm{rms}}$	15 A
	$< v >_{\mathrm{rms}}$	850 V

First, we consider the time-harmonic situation (see Figure 4.7) and find the Pareto front for the two conflicting objective functions

$$g_1(\boldsymbol{x}) = \overline{p}_{\mathrm{out}}(\boldsymbol{x}; \boldsymbol{c}) \,, \tag{4.2a}$$

$$g_2(\boldsymbol{x}) = \eta(\boldsymbol{x}; \boldsymbol{c}) \,, \tag{4.2b}$$

where $\overline{p}_{\mathrm{out}}$ is the (time averaged) power delivered to the load, η is the efficiency and $\boldsymbol{c}$ describes the design of the system in terms of fixed component values and other design parameters. In particular, the Pareto front of a circuit design with different values of the minimum distance d between the primary and secondary side and different load resistance R_L is shown in Figure 4.9. It is clear from Figure 4.9(a) that the system performance decreases rapidly with increasing distances, and we find that the distance should be at

[5]At 85 kHz, $\lambda/2 \approx 1750$ m in free space while the wire of a circular coil with 15 turns is approximately 17 m long.

most about 1.5 times larger than the maximum coil radius to achieve a power transfer of above 3.7 kW at an efficiency above 95 %. The load resistance does also influence the power transfer and efficiency, although to a lesser degree than the separation distance. It is noted that the constraints are satisfied and do not limit the optimization for the points along the Pareto fronts up to the sudden decrease in the efficiency that can be observed in Figure 4.9. At the decrease in efficiency, the active constraints are typically the generator current, the voltage and current product for the capacitor banks C_1 to C_3 and the current into C_4.

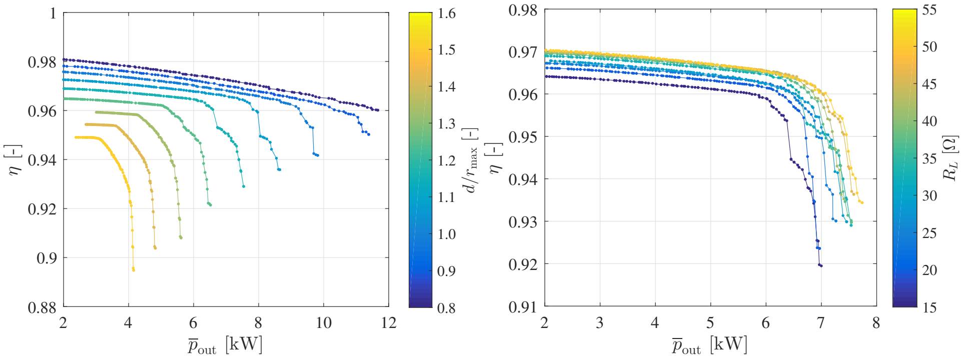

(a) Relative distance $d/r_{\max}$ **(b)** Load resistance R_L

Figure 4.9: Pareto fronts for different distance between the primary and secondary side expressed in terms of the maximum coil radius $r_{\max} = 0.25$ m in **(a)** and for different load resistance in **(b)**. The optimization is carried out for the time-harmonic case with $R_L = 35\,\Omega$ in **(a)** and $d/r_{\max} = 1.2$ in **(b)**.

Next, we consider the time-dependent scenario with the diode bridge and battery model shown in Figure 4.8 and a generator producing a square-wave input voltage with a maximum value of 450 V rms. The found Pareto fronts for the objective functions (4.2) are shown in Figure 4.10 for different values of the battery voltage and different power transfer distances. Here, a transfer distance of about $d/r_{\max} = 1.2$ is necessary to achieve a 3.7 kW power transfer at 95 % efficiency. This is a clear reduction from $d/r_{\max} = 1.5$ as found for the time-harmonic circuit with a resistive load. The main contributing factor to the reduced efficiency and power transfer is that the additional constraint on the current overtones in the first or last coil are active along the majority of the Pareto front. The maximum power transfer is, however, rather insensitive to the considered range of battery voltages. We also find that the optimized circuit parameters found for a high value of the battery voltage also performs rather well for the lower values of the battery voltage. Consequently, the presented IPT may be used to charge batteries with varying state-of-charge at a distance of up to 30 cm.

Additional results and optimized circuit parameters are presented in **Paper VI**.

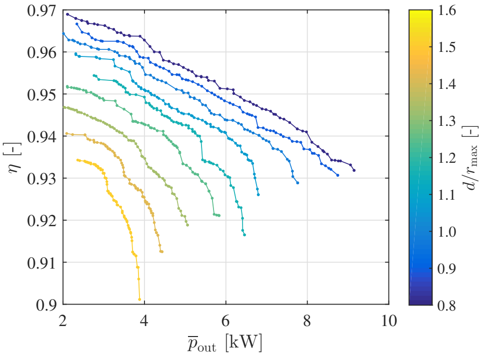

(a) Relative distance d/r

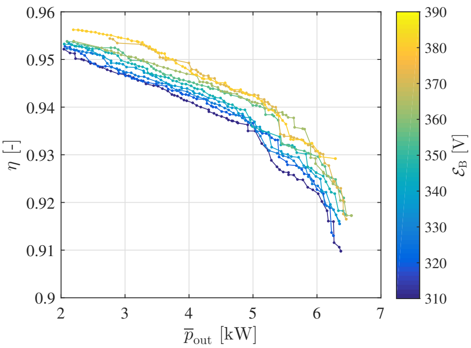

(b) Battery voltage $\mathcal{E}_{\mathrm{B}}$

Figure 4.10: Pareto fronts for different distance between the primary and secondary side expressed in terms of the maximum coil radius r_{max} = 0.25 m in **(a)** and for different battery voltages in **(b)**. The optimization is carried out for the time-dependent case with a battery load for $\mathcal{E}_{\mathrm{B}}$ = 380 V in **(a)** and d/r_{max} = 1.2 in **(b)**.

CHAPTER 5

CONCLUSIONS

The work presented in this thesis can be divided into three main parts: (i) a higher-order brick-tetrahedron hybrid finite element method (FEM) for Maxwell's equations; (ii) four inverse scattering problems associated with microwave based measurement systems; and (iii) the optimization of a wireless power transfer system based on inductively coupled resonant circuits for the automotive industry.

The higher-order brick-tetrahedron hybrid FEM employs Nitsche's method to enforce tangential continuity of the electric field in the weak sense at the interface between a structured grid of brick-shaped elements and an unstructured mesh of tetrahedrons. The hybrid method achieves h^{2p} convergence in the resonance frequencies for rectangular cavity problems without re-entrant corners or sharp edges. We demonstrate stable implicit-explicit time-stepping using an implicitness parameter associated with the tetrahedrons and the hybrid interface. No late-time instabilities have been observed for up to 300 000 time steps.

We present two microwave measurement systems and one numerical study. The first measurement system features an enclosed metal vessel with six rectangular waveguide ports. The measurement system is used to estimate the dielectric properties of moist micro-crystalline cellulose in terms of a Debye model, and we find that we can correlate the static permittivity and the relaxation time with the moisture content. Gradient-based optimization is used to minimize the misfit between the measured and computed scattering parameters. An adjoint field formulation is used to efficiently compute the gradients with respect to the Debye parameters. In another study, we use the same experimental equipment to detect and position up to five small scattering objects using a compressed sensing approach. Here, we use a dictionary containing the scattering parameters of a single scatterer placed at the grid points of a structured grid that spans the measurement region. This compressed sensing approach yields a 3 mm positioning accuracy for as many as five (well-separated) acrylic-glass cylinders based on only 20 frequency points in the frequency band from 2.7 GHz to 4.2 GHz.

The second measurement system is a monitoring system for a fluidized-bed process vessel used in the pharmaceutical industry, where we exploit the microwave resonances inside the process vessel. The measured perturbations of eight resonance frequencies are related to perturbations of the material process-state inside three different regions of the process vessel using an accurate three-dimensional numerical model of the process vessel. This estimation algorithm utilizes sensitivities of the measured resonance frequencies with respect to permittivity changes for the different regions inside the process vessel and we find that the monitoring system can successfully identify different process states and follow the evolution of the effective permittivity of the material distribution over the process time.

In the numerical study, we attempt to classify the size of intracranial bleedings for a simple two-dimensional head model by training a sub-space based classification algorithm on a large data set. Varying head size, head orientation, bleeding position and bleeding thicknesses are considered to model inter-patient variability for a total of 1250 different cases in six different classes. For an equally large validation set that features different head and bleeding sizes, we correctly identify the no-bleeding case with high accuracy and find a clear correlation between the bleeding thickness and the sub-space distance, which is the metric that the classifier bases its decision on.

Finally, we design and optimize an inductive power transfer system that is intended for charging batteries of stationary vehicles. Here, we consider a system with four coils in free space, where the coils are aligned along a common axis. For this situation, analytic results for the magnetic coupling are available, which significantly reduces the computational time needed to solve the optimization problem as compared to numerical computations. The currents and voltages in the circuit are subject to a number of constraints and a genetic algorithm is employed to find the optimal coil designs and capacitance values to achieve the maximum power transfer and efficiency. The Pareto fronts that contrast the power transfer and the efficiency are reported for (i) a time-harmonic circuit with a resistive load, and (ii) a non-linear circuit with square-wave excitation, rectifier, smoothing filter and battery. For the time-harmonic circuit, we find that a power transfer of above 3.7 kW at an efficiency above 95 % is possible to achieve for distances up to about 1.5 times the radius of the coils, where the outer radius of the (planar) coils is 25 cm. For the non-linear circuit, the transfer distance has to be reduced to approximately $d/r_{\max} = 1.2$ to achieve the same power transfer and efficiency as for the time-harmonic case. The reduced power and efficiency for the battery load is mainly attributed to the additional constraints that limits the current overtones in the coils. These overtones are excited by the square-wave generator and the rectifier circuit and can cause quasi-static magnetic fields that may damage or interfere with other electric systems in the vehicle.

REFERENCES

[1] T. Rylander, P. Ingelström, and A. Bondeson, *Computational Electromagnetics.* Texts in Applied Mathematics, New York: Springer, 3rd ed., 2013.

[2] Kane Yee, "Numerical solution of initial boundary value problems involving maxwell's equations in isotropic media," *IEEE Transactions on Antennas and Propagation*, vol. 14, pp. 302–307, may 1966.

[3] A. Taflove and S. C. Hagness, *Computational Electrodynamics: The Finite-Difference Time-Domain Method.* Artech House, third ed., 2005.

[4] A. Yefet and P. G. Petropoulos, "A Staggered Fourth-Order Accurate Explicit Finite Difference Scheme for the Time-Domain Maxwell's Equations," *Journal of Computational Physics*, vol. 168, pp. 286–315, apr 2001.

[5] V. A. Bokil and N. L. Gibson, "Analysis of spatial high-order finite difference methods for Maxwell's equations in dispersive media," *IMA Journal of Numerical Analysis*, vol. 32, pp. 926–956, jul 2012.

[6] J. C. Nedelec, "Mixed finite elements in R3," *Numerische Mathematik*, vol. 35, pp. 315–341, sep 1980.

[7] J. Jin, *The Finite Element Method in Electromagnetics.* Wiley-IEEE Press, 3rd ed., 2014.

[8] J. Webb, "Hierarchal vector basis functions of arbitrary order for triangular and tetrahedral finite elements," *IEEE Transactions on Antennas and Propagation*, vol. 47, no. 8, pp. 1244–1253, 1999.

[9] P. Ingelstrom, "A new set of H(curl)-conforming hierarchical basis functions for tetrahedral meshes," *IEEE Transactions on Microwave Theory and Techniques*, vol. 54, pp. 106–114, jan 2006.

[10] G. C. Cohen, *Higher-Order Numerical Methods for Transient Wave Equations.* Scientific Computation, Berlin, Heidelberg: Springer, 2002.

[11] T. Rylander and A. Bondeson, “Stability of Explicit-Implicit Hybrid Time-Stepping Schemes for Maxwell’s Equations,” *Journal of Computational Physics*, vol. 179, pp. 426–438, jul 2002.

[12] M. Bergot, G. Cohen, and M. Duruflé, “Higher-order Finite Elements for Hybrid Meshes Using New Nodal Pyramidal Elements,” *Journal of Scientific Computing*, vol. 42, pp. 345–381, mar 2010.

[13] D. Degerfeldt and T. Rylander, “A brick-tetrahedron finite-element interface with stable hybrid explicit-implicit time-stepping for Maxwell’s equations,” *Journal of Computational Physics*, vol. 220, pp. 383–393, dec 2006.

[14] N. Marais and D. B. Davidson, “Efficient High-Order Time Domain Hybrid Implicit/Explicit Finite Element Methods for Microwave Electromagnetics,” *Electromagnetics*, vol. 30, pp. 127–148, mar 2010.

[15] P. Hansbo, “Nitsche’s method for interface problems in computational mechanics,” *GAMM-Mitteilungen*, vol. 28, pp. 183–206, nov 2005.

[16] D. Nair and J. Webb, “Optimization of microwave devices using 3-D finite elements and the design sensitivity of the frequency response,” *IEEE Transactions on Magnetics*, vol. 39, pp. 1325–1328, may 2003.

[17] P. Jacobsson and T. Rylander, “Gradient-based shape optimisation of conformal array antennas,” *IET Microwaves, Antennas & Propagation*, vol. 4, no. 2, p. 200, 2010.

[18] A. Fhager and M. Persson, “Using a priori Data to Improve the Reconstruction of Small Objects in Microwave Tomography,” *IEEE Transactions on Microwave Theory and Techniques*, vol. 55, pp. 2454–2462, nov 2007.

[19] N. Nikolova, “Microwave Imaging for Breast Cancer,” *IEEE Microwave Magazine*, vol. 12, pp. 78–94, dec 2011.

[20] T. Halleröd, D. Ericsson, and A. Bondeson, “Shape and material optimization using gradient methods and the adjoint problem in time and frequency domain,” *COMPEL: The International Journal for Computation and Mathematics in Electrical and Electronic Engineering*, vol. 24, no. 3, pp. 882–892, 2005.

[21] M. Wahde, *Biologically Inspired Optimization Methods: An Introduction.* WIT Press, 2008.

[22] D. Donoho, “Compressed sensing,” *IEEE Transactions on Information Theory*, vol. 52, pp. 1289–1306, apr 2006.

[23] A. Massa, P. Rocca, and G. Oliveri, “Compressive Sensing in Electromagnetics - A Review,” *IEEE Antennas and Propagation Magazine*, vol. 57, pp. 224–238, feb 2015.

[24] A. Panahi and M. Viberg, “Fast LASSO based DOA tracking,” in *2011 4th IEEE International Workshop on Computational Advances in Multi-Sensor Adaptive Processing (CAMSAP)*, pp. 397–400, IEEE, dec 2011.

[25] L. C. Potter, E. Ertin, J. T. Parker, and M. Cetin, “Sparsity and Compressed Sensing in Radar Imaging,” *Proceedings of the IEEE*, vol. 98, pp. 1006–1020, jun 2010.

[26] G. Prisco and M. D’Urso, “Maximally Sparse Arrays Via Sequential Convex Optimizations,” *IEEE Antennas and Wireless Propagation Letters*, vol. 11, pp. 192–195, 2012.

[27] M. D. Migliore, “A Compressed Sensing Approach for Array Diagnosis From a Small Set of Near-Field Measurements,” *IEEE Transactions on Antennas and Propagation*, vol. 59, pp. 2127–2133, jun 2011.

[28] L. Poli, G. Oliveri, and A. Massa, “Microwave imaging within the first-order born approximation by means of the contrast-field bayesian compressive sensing,” *IEEE Transactions on Antennas and Propagation*, vol. 60, no. 6, pp. 2865–2879, 2012.

[29] A. M. Bruckstein, D. L. Donoho, and M. Elad, “From Sparse Solutions of Systems of Equations to Sparse Modeling of Signals and Images,” *SIAM Review*, vol. 51, pp. 34–81, feb 2009.

[30] E. Candes and M. Wakin, “An Introduction To Compressive Sampling,” *IEEE Signal Processing Magazine*, vol. 25, pp. 21–30, mar 2008.

[31] E. Nyfors, “Industrial Microwave Sensors—A Review,” *Subsurface Sensing Technologies and Applications*, vol. 1, no. 1, pp. 23–43, 2000.

[32] A. Toropainen, P. Vainikainen, and E. Nyfors, “Microwave Humidity Sensor for Difficult Environmental Conditions,” in *17th European Microwave Conference, 1987*, pp. 887–891, IEEE, oct 1987.

[33] L. Gradinarsky, H. Brage, B. Lagerholm, I. N. Björn, and S. Folestad, “In situ monitoring and control of moisture content in pharmaceutical powder processes using an open-ended coaxial probe,” *Measurement Science and Technology*, vol. 17, pp. 1847–1853, jul 2006.

[34] G. B. Gentili, C. Riminesi, and V. Tesi, “Low Cost Microwave Sensor for Moisture Content Measurement in Paper Milling Industry,” *Sensing and Imaging: An International Journal*, vol. 7, pp. 155–173, dec 2006.

[35] S. Y. Semenov and D. R. Corfield, “Microwave Tomography for Brain Imaging: Feasibility Assessment for Stroke Detection,” *International Journal of Antennas and Propagation*, vol. 2008, pp. 1–8, 2008.

[36] P. Heide and M. Vossiek, “24 GHz short-range microwave sensors for industrial and vehicular applications,” in *Short range radar*, pp. 1–7, 1999.

[37] B. Larsson, B. Bengtsson, and M. Gustafsson, “Nondestructive detection of decay in living trees,” *Tree Physiology*, vol. 24, pp. 853–858, jul 2004.

[38] D. Andreuccetti, R. Fossi, and C. Petrucci, “An Internet resource for the calculation of the dielectric properties of body tissues in the frequency range 10 Hz - 100 GHz,” 1997.

[39] C. Gilmore, P. Mojabi, A. Zakaria, S. Pistorius, and J. Lovetri, “On super-resolution with an experimental microwave tomography system,” *IEEE Antennas and Wireless Propagation Letters*, vol. 9, pp. 393–396, 2010.

[40] T. Cui, W. Chew, X. Yin, and W. Hong, “Study of Resolution and Super Resolution in Electromagnetic Imaging for Half-Space Problems,” *IEEE Transactions on Antennas and Propagation*, vol. 52, pp. 1398–1411, jun 2004.

[41] S. Gazit, A. Szameit, Y. C. Eldar, and M. Segev, “Super-resolution and reconstruction of sparse sub-wavelength images.,” *Optics express*, vol. 17, no. 26, pp. 23920–46, 2009.

[42] G. A. Covic and J. T. Boys, “Modern Trends in Inductive Power Transfer for Transportation Applications,” *IEEE Journal of Emerging and Selected Topics in Power Electronics*, vol. 1, pp. 28–41, mar 2013.

[43] M. P. Theodoridis, “Effective Capacitive Power Transfer,” *IEEE Transactions on Power Electronics*, vol. 27, pp. 4906–4913, dec 2012.

[44] J. Dai and D. C. Ludois, “Capacitive Power Transfer Through a Conformal Bumper for Electric Vehicle Charging,” *IEEE Journal of Emerging and Selected Topics in Power Electronics*, vol. 4, pp. 1015–1025, sep 2016.

[45] S. Y. R. Hui, W. Zhong, and C. K. Lee, “A Critical Review of Recent Progress in Mid-Range Wireless Power Transfer,” *IEEE Transactions on Power Electronics*, vol. 29, pp. 4500–4511, sep 2014.

[46] W. H. Ko, S. P. Liang, and C. D. F. Fung, “Design of radio-frequency powered coils for implant instruments,” *Medical & Biological Engineering & Computing*, vol. 15, pp. 634–640, nov 1977.

[47] M. W. Baker and R. Sarpeshkar, “Feedback Analysis and Design of RF Power Links for Low-Power Bionic Systems,” *IEEE Transactions on Biomedical Circuits and Systems*, vol. 1, pp. 28–38, mar 2007.

[48] X. Liu and S. Y. Hui, “Simulation study and experimental verification of a universal contactless battery charging platform with localized charging features,” *IEEE Transactions on Power Electronics*, vol. 22, no. 6, pp. 2202–2210, 2007.

[49] A. Kurs, A. Karalis, R. Moffatt, J. D. Joannopoulos, P. Fisher, and M. Soljacic, “Wireless Power Transfer via Strongly Coupled Magnetic Resonances,” *Science*, vol. 317, pp. 83–86, jul 2007.

[50] A. P. Sample, D. a. Meyer, and J. R. Smith, “Analysis, Experimental Results, and Range Adaptation of Magnetically Coupled Resonators for Wireless Power Transfer,” *IEEE Transactions on Industrial Electronics*, vol. 58, pp. 544–554, feb 2011.

[51] X. Wei, Z. Wang, and H. Dai, “A Critical Review of Wireless Power Transfer via Strongly Coupled Magnetic Resonances,” *Energies*, vol. 7, pp. 4316–4341, jul 2014.

[52] M. Kiani and M. Ghovanloo, “The Circuit Theory Behind Coupled-Mode Magnetic Resonance-Based Wireless Power Transmission,” *IEEE Transactions on Circuits and Systems I: Regular Papers*, vol. 59, pp. 2065–2074, sep 2012.

[53] J. L. Villa, J. Sallán, A. Llombart, and J. F. Sanz, “Design of a high frequency Inductively Coupled Power Transfer system for electric vehicle battery charge,” *Applied Energy*, vol. 86, pp. 355–363, mar 2009.

[54] R. Bosshard, J. W. Kolar, J. Muhlethaler, I. Stevanovic, B. Wunsch, and F. Canales, “Modeling and η-α-Pareto Optimization of Inductive Power Transfer Coils for Electric Vehicles,” *IEEE Journal of Emerging and Selected Topics in Power Electronics*, vol. 3, pp. 50–64, mar 2015.

[55] C. Park, S. Lee, G. H. Cho, and C. T. Rim, “Innovative 5-m-off-distance inductive power transfer systems with optimally shaped dipole coils,” *IEEE Transactions on Power Electronics*, vol. 30, no. 2, pp. 817–827, 2015.

[56] S. Kim, H.-H. Park, J. Kim, J. Kim, and S. Ahn, “Design and Analysis of a Resonant Reactive Shield for a Wireless Power Electric Vehicle,” *IEEE Transactions on Microwave Theory and Techniques*, vol. 62, pp. 1057–1066, apr 2014.

[57] J. Sallan, J. Villa, A. Llombart, and J. Sanz, “Optimal Design of ICPT Systems Applied to Electric Vehicle Battery Charge,” *IEEE Transactions on Industrial Electronics*, vol. 56, pp. 2140–2149, jun 2009.

[58] SAE Standard, “J2954, Wireless Power Transfer for Light-Duty Plug-In/Electric Vehicles and Alignment Methodology,” 2016.

[59] International Commission on Non-Ionizing Radiation Protection, “ICNIRP Guidelines for Limiting Exposure To Time-Varying Guidelines for Limiting Exposure To Time-Varying Electric, Magnetic and Electromagnetic fields,” *Health Physics*, vol. 74, pp. 494–522, 1998.

[60] J. D. Jackson, *Classical Electrodynamics.* New York: Willey, third ed., 1999.

[61] M. Bergot and M. Duruflé, “Approximation of H(div) with High-Order Optimal Finite Elements for Pyramids, Prisms and Hexahedra,” *Communications in Computational Physics*, vol. 14, pp. 1372–1414, nov 2013.

[62] COMSOL AB, “COMSOL Multiphysics®,” 2016.

[63] H. J. Liebe, G. A. Hufford, and T. Manabe, “A model for the complex permittivity of water at frequencies below 1 THz,” *International Journal of Infrared and Millimeter Waves*, vol. 12, pp. 659–675, jul 1991.

[64] T. Meissner and F. Wentz, “The complex dielectric constant of pure and sea water from microwave satellite observations,” *IEEE Transactions on Geoscience and Remote Sensing*, vol. 42, pp. 1836–1849, sep 2004.

[65] A. Sihvola, *Electromagnetic Mixing Formulas and Applications*, vol. 18. The Institution of Engineering and Technology, Michael Faraday House, Six Hills Way, Stevenage SG1 2AY, UK: IET, jan 1999.

[66] S. Boyd and L. Vandenberghe, *Convex Optimization.* Cambridge: Cambridge University Press, 2004.

[67] M. H. Wright, "The interior-point revolution in optimization: History, recent developments, and lasting consequences," *Bulletin of the American Mathematical Society*, vol. 42, pp. 39–57, sep 2004.

[68] J. Nocedal and S. J. Wright, *Numerical Optimization.* Springer Series in Operations Research and Financial Engineering, Springer New York, 2006.

[69] J. E. Dennis and R. B. Schnabel, *Numerical Methods for Unconstrained Optimization and Nonlinear Equations.* Society for Industrial and Applied Mathematics, jan 1996.

[70] K. Miettinen, *Nonlinear Multiobjective Optimization.* Springer Science & Business Media, illustrate ed., 1999.

[71] R. E. Steuer, *Multiple Criteria Optimization: Theory, Computation, and Application.* Krieger, reprint ed., 1986.

[72] K. Deb, *Multi-Objective Optimization Using Evolutionary Algorithms.* New York: John Wiley & Sons, Inc., 2001.

[73] J. B. Keller, "Inverse Problems," *The American Mathematical Monthly*, vol. 83, p. 107, feb 1976.

[74] V. G. Maz'ya and T. O. Shaposhnikova, *Jacques Hadamard: A Universal Mathematician.* American Mathematical Soc., 1999.

[75] A. Bondeson, Y. Yang, and P. Weinerfelt, "Optimization of Radar Cross Section by a Gradient Method," *IEEE Transactions on Magnetics*, vol. 40, pp. 1260–1263, mar 2004.

[76] P. M. van den Berg and A. Abubakar, "Contrast Source Inversion Method: State of Art," *Progress In Electromagnetics Research*, vol. 34, no. 9, pp. 189–218, 2001.

[77] R. O. Duda, P. E. Hart, and D. G. Stork, *Pattern Classification.* Wiley, 2000.

[78] Yinan Yu and T. McKelvey, "A subspace learning algorithm for microwave scattering signal classification with application to wood quality assessment," in *2012 IEEE International Workshop on Machine Learning for Signal Processing*, no. 3, pp. 1–6, IEEE, sep 2012.

[79] B. Lee and A. Newberg, "Neuroimaging in traumatic brain imaging," *NeuroRX*, vol. 2, pp. 372–383, apr 2005.

[80] M. R. Bullock, R. Chesnut, J. Ghajar, D. Gordon, R. Hartl, D. W. Newell, F. Servadei, B. C. Walters, and J. E. Wilberger, "Surgical Management of Acute Epidural Hematomas," *Neurosurgery*, vol. 58, pp. S2–7–S2–15, mar 2006.

[81] The MathWorks Inc., "Matlab®," 2016.